

RICE UNIVERSITY

Ion Trajectories in Mercury's Magnetosphere

by

Menelaos Sarantos

A THESIS SUBMITTED
IN PARTIAL FULFILLMENT OF THE
REQUIREMENTS FOR THE DEGREE

Doctor of Philosophy

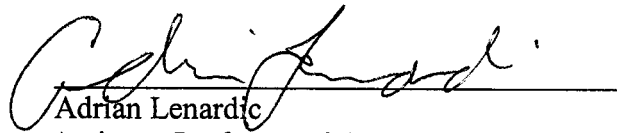
APPROVED, THESIS COMMITTEE:



Patricia H. Reiff, Chairman
Professor of Physics and Astronomy



Frank R. Tofoletto
Assistant Professor of Physics
and Astronomy



Adrian Lenardic
Assistant Professor of Geophysics

Houston, Texas

April, 2005

UMI Number: 3176074

INFORMATION TO USERS

The quality of this reproduction is dependent upon the quality of the copy submitted. Broken or indistinct print, colored or poor quality illustrations and photographs, print bleed-through, substandard margins, and improper alignment can adversely affect reproduction.

In the unlikely event that the author did not send a complete manuscript and there are missing pages, these will be noted. Also, if unauthorized copyright material had to be removed, a note will indicate the deletion.

UMI[®]

UMI Microform 3176074

Copyright 2005 by ProQuest Information and Learning Company.

All rights reserved. This microform edition is protected against unauthorized copying under Title 17, United States Code.

ProQuest Information and Learning Company
300 North Zeeb Road
P.O. Box 1346
Ann Arbor, MI 48106-1346

Abstract

Ion Trajectories in Mercury's Magnetosphere

By

Menelaos Sarantos

This thesis presents new tracings of ions in Mercury's magnetosphere that model the variability of the solar wind, sodium and potassium surface fluxes. The magnetic field is given from a modified version of the analytic Toffoletto-Hill (TH93) open magnetosphere model, which also gives the electric potential along open field lines. Its applicability is extended into the closed field line region by the Ding (1995) potential solver, which computes the realistic electric potential that is self-consistent with the magnetic field. Three cases of the solar wind and the interplanetary magnetic field (IMF) are tested, two at aphelion and one at perihelion. Photoions are launched from the scale height for each species, while solar wind ions are backtraced from the surface and to the magnetopause.

Photoion results reveal that the escape rate to the solar wind responds to external conditions only loosely: between aphelion and perihelion, the escape ratio was seen to range from 30 to just 40 percent. Therefore, impacts dominate. The prediction that recycling reduces by a factor of 1.5 at perihelion could help explain why the sodium atmosphere is denser at aphelion. The flux capable of sputtering varies between 10-15 % of the total dayside flux for strongly southward IMF $B_z = -10$ nT. In addition, tracings of Hermean ions show that differential escape losses do not exist for potassium photoions such that may explain the variable Na/K ratio in the Hermean atmosphere.

Solar wind ion tracings confirm that precipitation to Mercury's surface may happen along closed field lines not only at perihelion, but even at aphelion for realistic cases of southward IMF. The computed total sputtering flux increased by a factor of 1.7 from aphelion to perihelion. Most of the flux capable of sputtering is deposited on a region that is extended in longitude but limited in latitude. We conclude that ion sputtering caused by the solar wind can explain the high-latitude variability seen in imaging data of Mercury's sodium atmosphere.

This work is relevant to the NASA/Messenger and ESA/BepiColombo missions, both for mission planning and analysis of results.

Acknowledgments

This thesis is dedicated to my parents, Emmanouel and Aglaea, who brought me to where I am, and to my fiancée, Lysie, for her love, patience and support.

I would like to thank every member of my thesis committee for taking time to read this thesis and make meaningful comments. I am particularly indebted to my advisor, Pat Reiff; this thesis would not have been fruitful without her continuous guidance. Throughout the years that it took to complete this work, she has been a source of inspiration through both her expertise and, more importantly, her strong beliefs. Many warm thanks go to Frank Toffoletto for his assistance with the model, and to Adrian Lenardic for his thorough comments with regards to testing the finite element module.

Special recognition goes to Rosemary Killen, who has been the heart and soul of this project. Without her expertise this work would have been incomplete.

Thank you, Spyros Tsavachidis, my good friend, for helping out with MATLAB tasks. Many thanks to Andrew Urquhart who first modified the Toffoletto- Hill model to work at Mercury. Dimitris and Markos, thank you for making the grad school years the best time of my life so far.

Funding for this research was provided by NASA grants NAG5-11047 and NAG5-12566. Data for the Helios I and II analysis were obtained by *cohoweb*.

Contents

Abstract.....	
Acknowledgments.....	
Table of Contents.....	
1. Background.....	1
1.1 Introduction.....	1
1.2 Mercury's atmosphere: key issues.....	2
1.2.1 The sodium atmosphere: sources and sinks.....	3
1.2.2 Potassium and the problem of the variable Na/K ratio in Mercury's Atmosphere.....	7
1.2 Summary of tasks.....	8
2. The magnetosphere of Mercury.....	10
2.1 Introduction.....	10
2.2 Mercury's magnetosphere: variable and Earth-like.....	10
2.3 Modeling Mercury's magnetosphere.....	13
2.3.1 Predicting locations of ion sputtering.....	14
2.3.2 Modeling photoions.....	17

2.4 Summary.....	19
3. Methodology.....	21
3.1 Introduction.....	21
3.2 The Toffoletto – Hill (1993) magnetosphere model.....	22
3.3 The Ding potential solver.....	25
3.4 The particle tracer.....	28
3.5 Computing solar wind particle fluxes: the Onsager method.....	29
3.6 Limitations of the application of the TH93 model at Mercury.....	32
4. Photoion tracings.....	35
4.1 Objectives.....	35
4.2 Choices of particles and fields: implications of the Helios I and II datasets for the long-term variability in the environment of Mercury.....	36
4.3 Tracings of magnetic field lines with the TH93 model.....	41
4.4 Model photoion trajectories.....	45
4.5 Photoion fractional recycling and escape to the solar wind.....	47
4.5.1 Sodium and potassium global runs.....	48
4.5.2 The anisotropic atmosphere.....	56
4.6 Implications of photoion tracings.....	59

5. Tracings of solar wind ions.....	63
5.1 Overview.....	63
5.2 Predictions of solar wind precipitation fluxes.....	63
5.3 Implications of the solar wind mapping for Mercury's atmosphere.....	66
6. Summary.....	72
6.1 Photoions.....	72
6.2 Solar wind ions.....	74
6.3 Future work.....	75
References.....	78

CHAPTER 1: BACKGROUND

1.1 Introduction

This work quantifies production (via ion sputtering) and loss (via photoionization) of heavy species (e.g., Na, K) present in the exosphere of Mercury—specifically, production and loss that are regulated by the interaction of the magnetosphere with the solar wind. To this end, two types of ions are traced in Mercury’s magnetosphere: solar wind ions and photoions (or magnetospheric ions). The questions that this thesis addresses are:

- 1) Can solar wind ions eject fresh neutrals from Mercury’s surface in sufficient rates to maintain the observed atmospheric densities?
- 2) Can photoions efficiently recycle to the surface and allow a buildup of the sputtered atmosphere or redistribute volatiles on the surface?

To answer these questions, a full-particle tracing code was developed to follow thousands of ions in Mercury’s magnetosphere. The Toffoletto-Hill (1993) model of the Earth’s magnetosphere was modified to describe the magnetic and electric field configuration at Mercury. Using this model, this research computes the flux intensity and energy distributions of impacting solar wind and magnetospheric ions for different solar wind (aphelion to perihelion) and interplanetary magnetic field (IMF) conditions to determine how many of these ions cause sputtering (solar wind ions; photoions) or recycle (photoions).

When we understand how the magnetosphere affects the atmosphere of Mercury, we will understand why ions must be traced. Chapters 1 and 2 delineate the key issues related to the two major themes of this work, the atmosphere and the magnetosphere of Mercury, and explain how they are coupled. Chapter 3 describes the models which were used for this work and details how they were successfully modified for Mercury. Chapter 4 presents the results of the photoion tracings and discusses their implications for Mercury's atmosphere. Chapter 5 delivers computations of solar wind ion sputtering. Finally, Chapter 6 summarizes our results and outlines the direction of future work.

1.2 Mercury's atmosphere: key issues

Mercury has a tenuous atmosphere, which is technically an exosphere: the mean free path of an atmospheric neutral is comparable to the exosphere's scale height. While six elements have been observed in the Hermean exosphere, namely H, He, O, Na, K, and Ca, only the sodium and potassium exospheres have been monitored over long timescales. Mercury's sodium and potassium exospheres exhibit rapid changes (on timescales less than an Earth day), and high- and mid-latitude enhancements (Potter and Morgan, 1990; 1997; Potter et al., 1999). In contrast, little is known about the time variability of other species. For these reasons, sodium and potassium will define this work.

1.2.1 The sodium atmosphere: sources and sinks

Images of the Na exosphere show that bright spots of sodium emission are often seen at high- and mid- latitudes, and that these spots are often brighter in one hemisphere (e.g.,

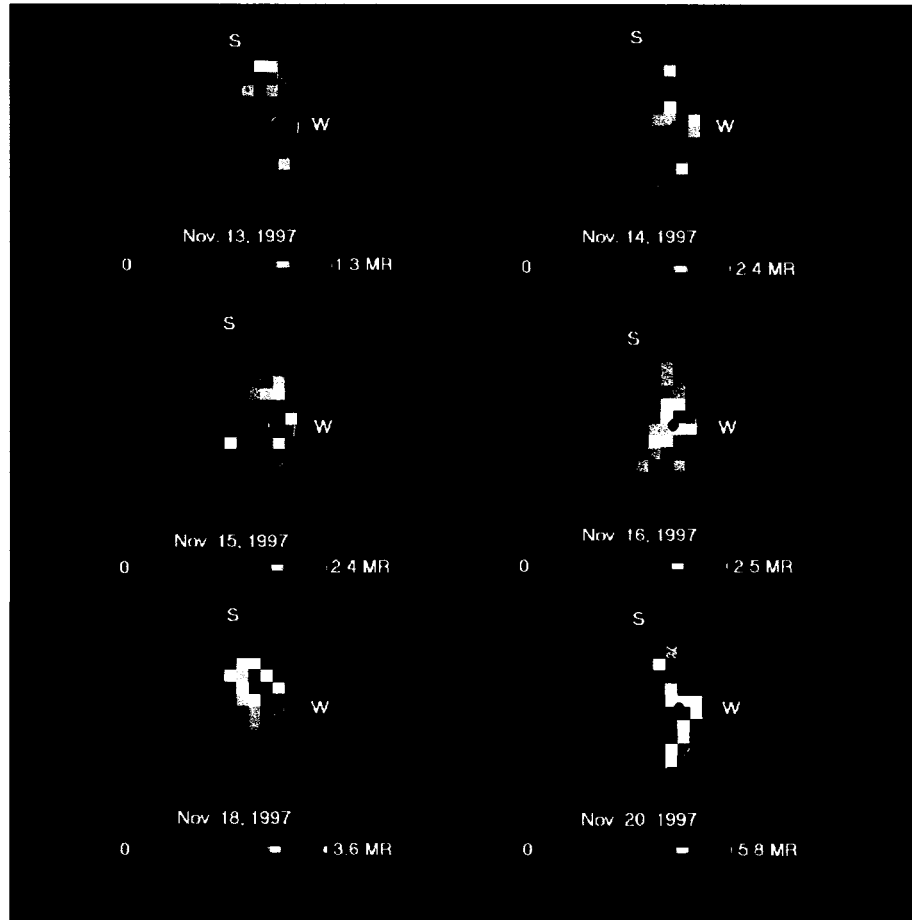


Figure 1.1: The sodium atmosphere of Mercury observed on November 13-20, 1997. High- latitude enhancements of emission are seen from November 15 on. The overall content of the atmosphere increased by a factor of two during the week. This rapid variability is likely the effect of increased ion sputtering, which is modeled in this thesis. (From Killen et al., 2001)

Killen et al., 2001). At least one data set has been reported (Sprague et al, 1997) that shows an asymmetry in Na column abundance between the dawn (morning) and dusk

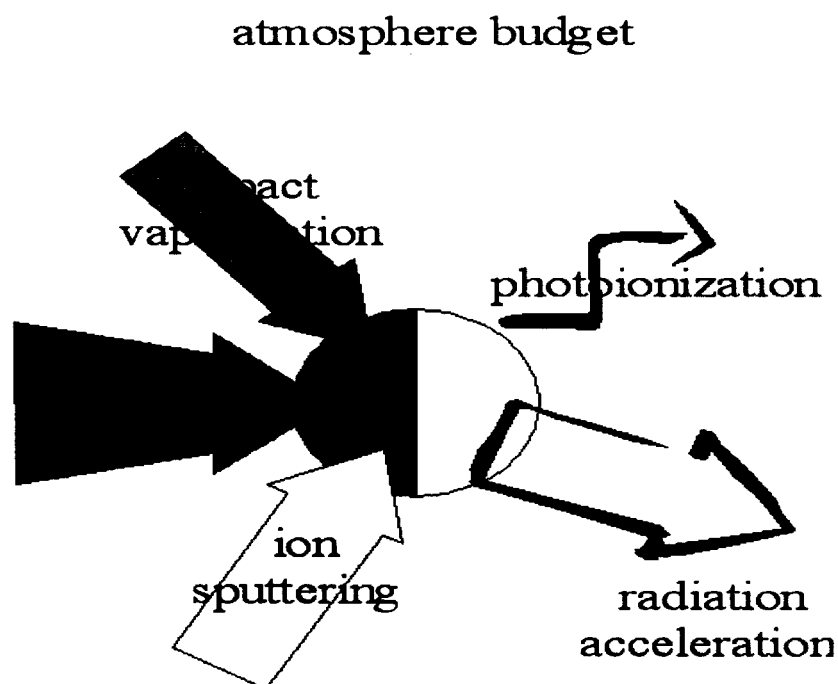


Figure 1.2: Suggested source and loss mechanisms for Mercury's sodium and potassium atmosphere.

(afternoon) sectors. However, Killen and Morgan (1993) reported that bright spots are as likely on the evening as on the morning side.

Why are these high-latitude enhancements enigmatic? Four suggested source processes form and maintain Mercury's atmosphere: photon-stimulated desorption, thermal vaporization, impact vaporization and ion sputtering. Because thermal and photon-induced desorption, the first and second suggested source mechanisms, vary with longitude and latitude at Mercury's surface, they produce atmospheric neutrals mainly around the subsolar point (low latitudes). While impact vaporization, the third mechanism, which is caused by micrometeoroids, provides roughly 25% of the source, it is uniformly distributed (Killen et al., 2001). This thesis tests the hypothesis that high-

latitude enhancements are caused by solar wind ions that penetrate to the surface along open (or closed) field lines of Mercury's magnetosphere and eject surface-bound neutrals, a process known as ion sputtering.

Also enigmatic is the rapid variability of Mercury's sodium atmosphere. If the atmosphere and magnetosphere of Mercury were not coupled, or if the magnetosphere and the solar wind were constant, production and loss should vary smoothly about the orbit of Mercury. Smith and Marconi (1995) calculated that, theoretically, under these conditions, the content of the sodium atmosphere of Mercury should vary by a factor of 1.6 over its orbit. But observations made on successive days show that Mercury's exosphere actually varies rapidly both in morphology and in total content. The spatial distribution changes daily; the total sodium content also changes daily and has been observed to triple in just a week (Killen et al., 2001). These variations, which in a week are larger than variations predicted for the entire orbital period (87 days), possibly happen when Coronal Mass Ejection (CME) events intersect Mercury's orbit. During a CME event, the solar wind is accompanied by a strong southward IMF while its speed can exceed 800 km/sec.

To explain the rapid variability and high latitude enhancements seen in Mercury's exosphere, two mechanisms have been proposed. One explanation might be that these features are caused by variations (local enhancements) in the underlying terrain, specifically, the Caloris basin (Sprague et al., 1998). But, as Killen and Morgan (1993) remark, at least some enhancements are not related to surface features (e.g., Killen et al., 2001). The other explanation, suggested by Potter and Morgan (1990), is that the variability and high-latitude enhancements are caused by the interaction of the solar wind

with Mercury's magnetosphere, which is variable on timescales unrelated to the orbital position. It is these magnetospheric effects that this thesis models.

Even the most important source mechanism is contested. Killen et al. (2001) computed that, although photon-stimulated desorption (PSD) is the primary mechanism that maintains the atmosphere, ion sputtering can account for up to 32% of the sodium content depending on solar wind and IMF conditions. However, the importance of ion sputtering was challenged by Leblanc and Johnson (2003). They used a different model of Mercury's surface to conclude that the subsolar surface, responding mainly to thermal vaporization, becomes rapidly depleted in volatiles, but that the high-latitude surface areas, which have a smaller temperature, can sustain the atmosphere longer. Because Mercury's exosphere is surface-bounded, predicting the relative importance of the proposed source mechanisms depends on the model of Mercury's surface used. But any attempt to model all source and loss mechanisms concurrently should include a magnetosphere model, and this work covers this need.

The loss processes for atmospheric sodium on the dayside are photoionization and migration to the nightside due to acceleration of neutrals by solar radiation pressure. At Mercury the primary loss mechanism for all atoms heavier than He is photoionization. Specifically, the sodium lifetime against photoionization varies between 3 hours (perihelion) and 10 hours (aphelion), while it can be as short as 1.5 hours under active solar conditions. Resulting photoions, which may either impact the surface or cross the magnetopause and escape to the solar wind, can change the atmosphere in more than one way. For one, photoions, like the more energetic solar wind ions, can also cause sputtering when they impact the surface provided that they are accelerated by the electric

field of the magnetosphere to impact energies >300 eV. More importantly, as suggested by Killen et al. (2001) and Potter et al. (2002), high photoion recycling rates ($>10\%$ of photoion flux) may allow the sputtered atmosphere to grow steadily. By launching thousands of dayside photoions in Mercury's magnetic and electric fields, this research computes the energy distribution of impacting photoions to quantify secondary sputtering; it also computes for the first time global recycling rates for sodium and potassium photoions for solar wind and IMF conditions at perihelion and at aphelion.

1.2.2 Potassium and the problem of the variable Na/K ratio in Mercury's atmosphere

Because the variability of the Na/K ratio in the atmosphere remains unexplained, this thesis focuses on comparing different photoion species in Mercury's atmosphere and examines whether larger photoion losses exist for potassium.

The Na/K ratio in the atmosphere is variable. Long-term observations compiled over the last 17 years indicate that when atmospheric sodium increases, potassium also increases, and vice versa, but that they do not maintain the same ratio. While the cosmic Na/K ratio is about 20, and the ratio of Na/K in the exosphere of the Moon is about 7 (roughly the ratio of Na/K in the lunar rocks), measured values of the Na/K ratio in Mercury's atmosphere are much higher and vary between 40 and 160 (Potter et al., 2002).

The variability and high values of Mercury's Na/K ratio may be an indication that loss processes for sodium and potassium have different efficiencies. While radiation

pressure varies with Mercury's True Anomaly Angle (TAA=0 at perihelion; TAA=180 at aphelion), it does not affect the Na/K ratio in the atmosphere because it acts nearly "stoichiometrically" on these two species (Potter et al., 2002). On the other hand, photoionization losses depend on a) the photoionization rate; and b) the fractional rate of resulting ions that recycle to the surface. When Mercury moves from aphelion ($r=0.47$ AU) to perihelion ($r=0.31$ AU), the photoionization rate increases as $1/r^2$; but the fraction of resulting ions that return to the surface and neutralize may also vary, because the magnetosphere, which regulates ion recycling, is under stronger solar wind and IMF conditions at perihelion. Potter et al. (2002) suggested that recycling rates for potassium photoions will be lower than recycling rates for sodium photoions because potassium has a larger gyroradius in Mercury's magnetic field. By computing global recycling rates for sodium and potassium photoions, this work models for the first time how the larger gyroradius of K^+ ions affects the atmospheric Na/K ratio through increased loss of potassium, and tests the hypothesis that the efficiencies of photoion recycling for sodium and potassium significantly differ between perihelion and aphelion. In particular, these are the first ever global tracings for potassium photoions.

1.3 Summary of tasks

To compute the variability of the ion sputtering rate at Mercury's surface, this research traces solar wind and magnetospheric ions in Mercury's magnetosphere under a number of solar wind and IMF conditions. Tracings of magnetospheric ions also quantify the global recycling rate for sodium and potassium photoions that impact the surface and

neutralize, and investigate whether differential escape losses exist for potassium photoions such that may explain the variable Na/K ratio in the Hermean atmosphere.

CHAPTER 2:

THE MAGNETOSPHERE OF MERCURY

2.1 Introduction

Mercury's magnetosphere appears Earth-like and is extremely variable. It is characterized by its compact size, weak ionosphere leading to increased reconnection efficiency with the IMF, an extremely variable solar wind environment, and short photoionization and convection time scales. As a result, although models of the Earth's magnetosphere can be applied to simulate the magnetosphere of Mercury, they should be carefully modified. The existence of a magnetosphere surrounding Mercury critically affects the way Mercury's tenuous atmosphere interacts with the solar wind. Previous and current efforts to model the solar wind – magnetosphere interaction and the photoion recycling will be discussed.

2.2 Mercury's magnetosphere: variable and Earth-like.

Mariner 10, the only spacecraft ever to visit the vicinity of Mercury, concluded that Mercury has a magnetosphere. The first flyby, in March 1973, was a nightside passage with a distance at closest approach of 707 km ($0.3 R_M$) from the planet's surface. The magnetometer measurements suggested the existence of an intrinsic dipole field (Ness et

al., 1975). A second flyby, designed to give good visual contact with the planet, was well outside the planetary magnetosphere. However, a third flyby in March 1974 at a nightside distance of 327 km ($0.1 R_M$) gave strong evidence in favor of a terrestrial-like dipole field. Using a simple closed magnetosphere model, Ness et al. (1975) estimated Mercury's magnetic moment to be about $350 \text{ nT } R_M^3$ ($\sim 7 \times 10^{-4}$ weaker than that of the Earth.) Later, a number of authors attempted to improve these results by using more elaborate models (see, e.g., Jackson and Beard, 1977; Whang, 1977). They obtained estimated moments that differ almost by a factor of two. The dipole of Mercury has the same polarity as the Earth's at present, with a dipole tilt very close to zero degrees. These Mariner 10 observations suggest an Earth-like magnetosphere, a finding that allows the use of a model of the Earth's magnetosphere such as Toffoletto-Hill (1993), appropriately modified, to simulate the Hermean system.

While Mercury's magnetosphere bears similarities with that of the Earth, it is different in many important ways. First, the Hermean magnetosphere is small; a simple pressure balance between the solar wind pressure and the planetary magnetic pressure gives a magnetosphere whose linear dimensions are about 6-7% of those of the Earth (Russell et al., 1988). Second, because Mercury occupies a larger fraction of its magnetospheric volume compared to the Earth, the structure of Mercury's inner magnetosphere, an area typically comprising features such as the plasmasphere, the ring current and the radiation belts at the Earth, is simplified (Russell et al., 1988). Third, unlike conditions at the Earth, Mercury's low atmospheric density ($<10^6 \text{ cm}^{-3}$ at the surface) results in a dynamically insignificant ionosphere (Hill et al., 1976). Because of the lack of a conducting ionosphere, reconnection of the IMF with Mercury's magnetic

field is believed to be twice as efficient as is estimated for the Earth's magnetosphere under similar solar wind conditions (Slavin and Holzer, 1979). All this is important knowledge that was used during the setup of the magnetosphere model for this work.

But the most important difference in Mercury's magnetosphere is the dominance of the radial component (B_x) of the IMF. The IMF cone angle of the Parker nominal field with respect to the radial direction is only $\sim 20^\circ$ for typical solar wind conditions at 0.3 – 0.5 AU; compared to the Earth's 45° , this results in B_x being on average the largest of all three components of the IMF. This condition has a dramatic effect on the magnetospheric configuration, an effect that will be discussed extensively in part (2.3.1) of this chapter. Unlike other models, the Tofolletto-Hill (1993) model that is used in this work can successfully handle the all-important B_x component.

If the magnetosphere of Mercury is responsible for the observed (rapid) variability of the Hermean atmosphere, it must, too, be rapidly variable. Because the boundaries of the magnetospheric system are measured on scales of one planetary radius or less (e.g. Ness et al., 1975; Ogilvie et al., 1977; Kabin et al., 2000; Sarantos et al., 2001), and because the convection time scale is of the order of one minute (e.g., Killen and Ip, 1999), the solar wind-Hermean system is expected to show more dramatic and more rapid changes than the solar-terrestrial analog: while the Earth's magnetosphere takes ~ 20 -40 minutes to respond to an IMF reconfiguration, Luhmann et al. (1998) suggested that "Mercury's magnetosphere is so small that it can establish a new configuration on the order of the nominal solar-wind transit time past it of ~ 1 minute". Mercury also has a very eccentric orbit, with a perihelion at 0.31 AU and an aphelion at 0.47 AU; this large eccentricity results in solar wind and IMF conditions that vary greatly depending on the position of

the planet along its orbit. These conditions lead to a highly variable response of Mercury's magnetosphere.

2.3 Modeling Mercury's magnetosphere

Four basic types of magnetosphere models have been developed for Mercury and used to study the solar wind interaction with the magnetosphere: three analytic models (Luhmann et al., 1998; Sarantos et al., 2001; Delcourt et al., 2002; 2003), a semi-empirical model (Massetti et al., 2003), a quasi-neutral hybrid model (Kallio and Janhunen, 2003), and two MHD models (Kabin et al., 2000; Ip and Kopp, 2002). In broad terms their predictions agree: because Mercury's magnetic field is small, and its atmosphere is tenuous, solar wind ions can hit Mercury's surface along open field lines (magnetic lines that have one end connected to the solar wind). The footprint of open magnetic field lines ("cusp") contracts or expands responding mainly to changes in the IMF. Hence, the IMF, which is variable, regulates the ion sputtering rate and the related atomic sodium (or potassium) emission, which are therefore also variable. However, predictions of different models regarding the extent of the cusps and the amount of the plasma reaching the surface differ.

In the following paragraphs we will summarize the current state of our knowledge regarding the modeling of ions in Mercury's magnetosphere, and show how this work fits into the broader context.

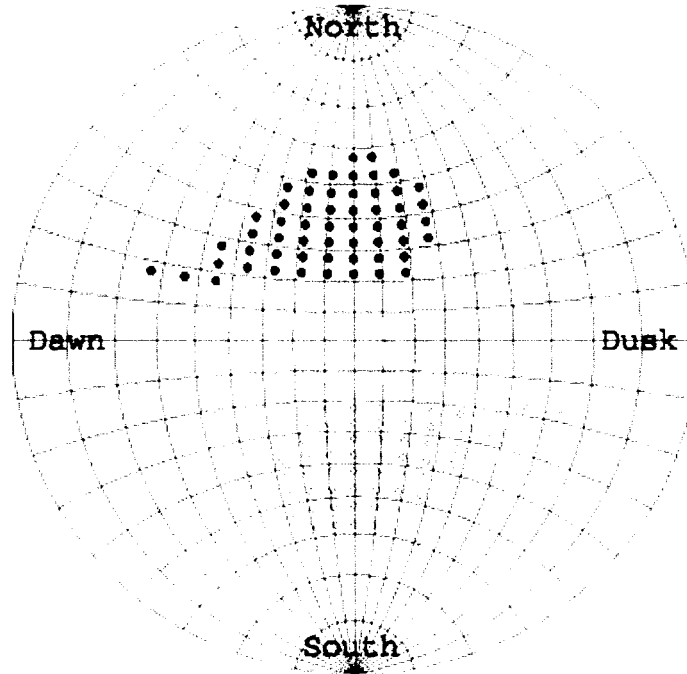


Figure 2.1: Footprint of open field lines on Mercury's surface for the case $B_x = -40$ nT, $B_y = -5$ nT, $B_z = -20$ nT. When the IMF B_x and B_z are both strong, the open field line area (impact region) maps close to the equator. Full circles (•) represent open lines that are turned towards the solar wind (sunwards), while diamonds (◊) denote open field lines that are turned antisunward. (Adapted from Sarantos et al., 2001)

2.3.1 Predicting locations of ion sputtering

Early work traced magnetic field lines in Mercury's magnetosphere to predict sputtering locations of solar wind ions. Following the suggestion by Luhmann et al. (1998) that Mercury's magnetosphere restructures itself rapidly when the IMF changes, Killen et al. (2001) and Sarantos et al. (2001) used the Toffoletto-Hill (1993) model to compute regions of open field lines (cusps) as a function of the direction of the IMF and of the solar wind dynamical pressure at Mercury. They concluded that the size of

Mercury's cusps is extremely sensitive to the interplanetary magnetic field, and predicted that a large part of the planetary surface is open to the solar wind when the IMF B_z is southward. More cases of the IMF clock angle were tested by Ip and Kopp (2002) showing that, when the IMF is straight southward, the open-closed boundary (lower limit of the cusp) could be pushed equatorward to about 30 degrees north or south latitude. When the radial component of the IMF is dominant, most of the precipitating solar wind ions impact on one hemisphere: for a sunward-pointing component ($B_x > 0$) most ions reach the surface of Mercury's southern hemisphere; the opposite is true for an antisunward-pointing field ($B_x < 0$). This north-south asymmetry was first pointed out by Sarantos et al. (2001) who qualitatively showed that, for a negative B_x , solar ions have a velocity component parallel to Mercury's (open) magnetic field configuration in the northern hemisphere but antiparallel in the southern hemisphere, and vice versa. To quantify this, Kallio and Janhunen (2003) tested one case of a Parker IMF ($B_x = 32$ nT, $B_y = 10$ nT, $B_z = 0$ nT). They found that in that case only 36% of the total proton flux impacted the northern hemisphere. This result implies that when there is a north-south asymmetry of the sputtering emissions in the atmosphere, an upper limit of a 2:1 ratio of total content in each hemisphere should be expected.

These models all agree that it is the IMF direction, not the solar wind pressure, that critically determines the extent of the cusps (Killen et al., 2001; Ip and Kopp, 2002; Massetti et al., 2003). But, to calculate the optical emission, we must compute the solar wind particle flux that reaches Mercury's surface.

More recently, solar wind particle fluxes at the surface have been calculated (Massetti et al., 2003; Kallio and Janhunen, 2003). Massetti computed that, for an IMF $B_z = -10$

nT, a mean proton flux of $4.1 \times 10^8 \text{ cm}^{-2} \text{ s}^{-1}$ impacts Mercury's surface along open field lines. This compares well to the maximum rate per unit area for PSD ($2.5 \times 10^7 - 6 \times 10^7 \text{ cm}^{-2} \text{ s}^{-1}$) making ion sputtering a comparatively important source for Mercury's atmosphere. Using a similar estimate, Killen et al. (2001) calculated that up to 32% of the sodium atmosphere content comes from ion sputtering along open field lines when the IMF is southward. But Kallio and Janhunen found that extensive proton precipitation happens equatorward of the open-closed boundary, that is, along closed field lines, even for relatively “quiet” solar wind conditions. In fact, these authors predicted that, when the solar wind speed is about 860 km/s (during a CME event, for example), energetic solar wind ions reach even the subsolar area because their gyroradius (0.38 R_m) becomes comparable to the (small) magnetopause distance above the surface of the planet.

However, as Table 2.2 asserts, only seven cases of solar wind fluxes have been modeled to date. These cases all tested either perihelion conditions ($N = 76 \text{ cm}^{-3}$) or extreme conditions ($N_{sw} = 100 \text{ cm}^{-3}$; $v_{sw} = 600\text{-}800 \text{ km s}^{-1}$) for the solar wind, and exploratory conditions for the IMF. They tell us nothing about how often these configurations occur. To complement these results, a more systematic approach is needed that establishes the most probable ion sputtering rate at Mercury's extreme orbital points. This research uses the results of a new analysis of the long-term particle and field environments of Mercury obtained through the Helios I and II spacecrafts to predict the most likely configurations of southward IMF. With these likely boundary conditions for the magnetosphere, we trace solar wind ions and quantify the solar wind flux that reaches Mercury's surface both at perihelion and aphelion.

IMF[B _x ,B _y ,B _z](nT)	V _{sw} (km s ⁻¹)	N _{sw} (cm ⁻³)	Authors
[0,0,10]	430	76	Kallio and Janhunen (2003)
[0,0,-10]	430	76	Kallio and Janhunen (2003)
[30, 10, 0]	430	76	Kallio and Janhunen (2003)
[0,0,10]	860	76	Kallio and Janhunen (2003)
[x,0,-10]	400	60	Masetti et al. (2003)
[x,-5,-10]	400	60	Masetti et al. (2003)
[x,-5,-10]	600	100	Masetti et al. (2003)

Table 2.2: Published runs that computed solar wind fluxes at Mercury's surface

2.3.2 Modeling photoions

Although some progress has been achieved on tracing solar wind ions, little has been done on tracing photoions. Tracings of ion trajectories depend on the species' mass, initial position, and configuration of magnetic and electric fields in Mercury's magnetosphere. Trajectories that have been computed for Na⁺ (Ip, 1987; 1993; Delcourt et al., 2002; Killen et al., 2003) show that magnetospheric ions are not always bound to magnetic field lines.

When Ip (1987; 1993) modeled trajectories of Mercury's heavy ions, he found that some photoions neutralize when they impact the surface, while others cross the magnetopause and escape to the solar wind. But Ip assumed the simplest possible representation for the electric field, namely a uniform dawn-to-dusk electric field

throughout the magnetosphere, and launched just a few ions mainly from the nightside. Delcourt et al. (2002) launched sodium ions from dayside high latitudes (70° and 85° invariant latitude near noon) and found that such particles were $\mathbf{E} \times \mathbf{B}$ –accelerated to energies of about 4 keV before they reimpacted the nightside surface of Mercury. However, these papers tell us nothing about the long-term consequences of ion recycling because they are based on a limited choice of trajectories and IMF configurations, and do not compute the global recycling rates for all dayside photoions.

In Killen et al. (2003), we first quantified the global recycling rate for Na^+ ions when we launched about 3,500 ions from Mercury’s dayside surface. Even though ions launched at low altitudes (< 10 km) account for only $\sim 10\%$ of all photoions, we found that up to 60% of sodium photoions impact the surface and neutralize, and reported a dawn-dusk asymmetry in the recycling efficiency: about four times more particles returned to the dawn side than to the dusk sector. This prediction may explain data sets in which the average column densities of Na and K atmospheric neutrals are higher in the dawnside (Sprague *et al.*, 1997). Delcourt et al. (2003) forecasted that recycling accounts for only 15% of all ions. This research adds to previous results by launching sodium and potassium ions not only from the surface, but from shells located at the scale height altitude of the atmosphere. This is the first work to establish comparative recycling rates for sodium and potassium photoions launched under different IMF conditions (perihelion to aphelion).

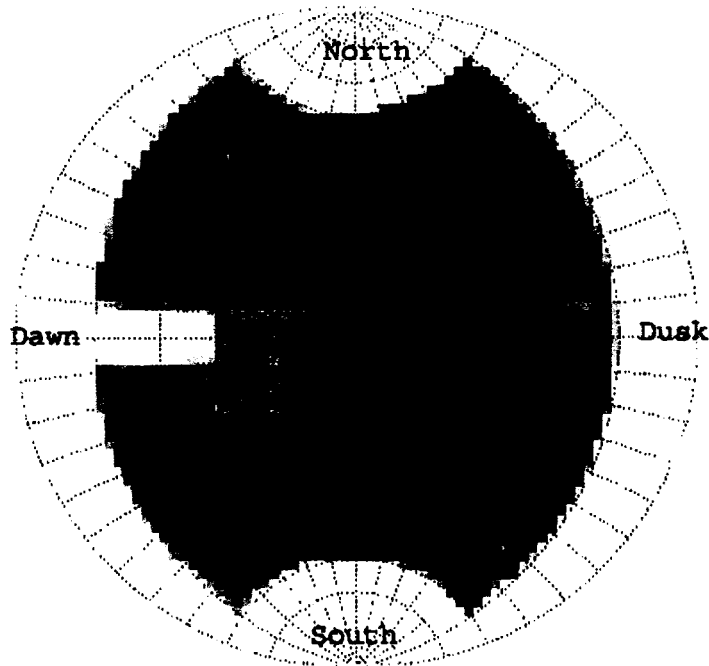


Figure 2.2: Na^+ redistribution pattern for IMF $[-30,15,-10]$ nT. 3,500 particles were launched from the surface with an isotropic spatial distribution. Color coded is the (dayside) fractional recycling ratio, which is four times higher in the dawn than it is in the dusk sector. (Adapted from Killen et al., 2003)

2.4 Summary

Only seven cases of solar wind proton and three cases of global photoion tracings have been published to date. This thesis presents three new tracings of solar wind ions (H^+) and six new tracings of magnetospheric ions (Na^+ and K^+) in Mercury's magnetosphere. While previous cases were based on exploratory choices for the solar wind and did not tell us how often these conditions happened, this work, capitalizing on Rosemary Killen's recent analysis of the Helios I and II datasets for Mercury's orbital

distances (Killen, personal communication), systematically establishes the most probable ion sputtering rate at Mercury's extreme orbital points. Results are analyzed to evaluate the relative importance of ion sputtering as a source mechanism for Mercury's atmosphere, as well as to understand the variability of the Na/K ratio in the atmosphere of Mercury.

CHAPTER 3:

METHODOLOGY

3.1 Introduction

This thesis computes a large number of ion trajectories in Mercury's magnetosphere in order to determine by how much solar wind ions contribute to the atmospheric source, and to quantify how often photoions escape to the solar wind or return to the surface. Because these ions respond to gravity and electromagnetic forces, the particle tracer developed in this work requires modeled input for the magnetospheric magnetic and electric fields. The magnetic field is given from a modified version of the analytic Toffoletto-Hill (TH93) open magnetosphere model, which also gives the electric potential along open field lines. Its applicability is extended into the closed field line region by the Ding (1995) potential solver, which computes the realistic electric potential that is self-consistent with the magnetic field. Following is a description of these models, as well as an account of the modifications that were applied to them in order to accurately describe the fields at Mercury.

While photoion fluxes that impact the surface can easily be computed in our particle tracer given the average atmospheric column abundance and the ionization lifetime, to establish the contribution of solar wind particles to ion sputtering we modified the Onsager (1993; 1995) mapping method. The essence of this scheme, and the appropriate modifications to fit this work, will also be described in this chapter.

3.2 The Toffoletto-Hill (1993) magnetosphere model

The TH93 model is a steady-state open magnetospheric model for the Earth. By “steady-state” we mean that the model is effectively viewing the magnetospheric configuration in a time averaged sense, not seeking to describe the configuration at any given time (Vasyliunas, 1983). In other words, the model successfully describes the magnetosphere as long as averaging timescales are longer than the convection time scale, a condition which is very appropriate at Mercury where the convection timescale is of the order of one minute.

The TH93 model builds on the Voigt (1981) model of the Earth’s closed magnetosphere. In the Voigt model, as well as in TH93, the shape of the magnetopause consists of a hemisphere on the dayside attached to a semi- infinite cylinder on the nightside which represents the magnetotail. While the standoff distance of the dayside magnetopause is flexible responding to the solar wind and magnetic field pressures, elsewhere this prescribed magnetopause is not the outcome of a detailed pressure balance between the solar wind and the magnetospheric field. Instead, it reasonably approximates the shape of the magnetopause. The main advantage of this geometry is that it enables analytical solutions of the Laplace equation.

Whereas the main interior field of the Voigt model is a dipole, this term is supplemented with a term describing the tail field. In order to represent the elongation of the tail field, the dipole field is stretched in the cylinder by multiplying the two field components that are perpendicular to the tail axis by a parameter α . The $\alpha=1$ case

represents no stretching, whereas all values between zero and one describe geometries in which the magnetic field decays rapidly with increasing distance down the tail. Realistic configurations of the tail are achieved with $\alpha=0.05-0.20$ (Toffoletto and Hill, 1989), and a value of $\alpha=0.15$ is employed in this work.

In a closed magnetosphere model, such as the Voigt model, the magnetopause field \mathbf{B}_{CF} shields all interior terms. Because this field is curl-free inside the magnetopause, it can be described by a harmonic scalar potential Φ_{CF} :

$$\mathbf{B}_{CF} = -\nabla\Phi_{CF} \quad (3.1a)$$

with

$$\nabla^2\Phi_{CF} = 0 \quad (3.1b)$$

This potential satisfies a Neuman boundary condition, namely that everywhere on the magnetopause the normal component of the shielding field \mathbf{B}_{CF} cancels the normal component of the internal field:

$$-\frac{\partial\Phi_{CF}}{\partial n} = (\mathbf{B}_{INT})_n \quad (3.2)$$

Thus, as a natural outcome of a closed model, the normal magnetic field at the magnetopause is zero everywhere.

As mentioned before, the TH93 model builds on the Voigt model with two critical additions: 1) the introduction of a normal component that opens the magnetosphere; and 2) the introduction of an “additional tail field” term which succesfully “shields” the modified interior field.

To produce the desired open field configuration in the TH93 model, a so-called “interconnection field” \mathbf{B}_{IF} was added as a perturbation to the closed magnetic field

model. In the TH93 model, the interconnection field is defined as the unique magnetic field that satisfies the boundary conditions, is divergence-free everywhere, and is curl-free everywhere except at the magnetopause:

$$\mathbf{B}_{IF} = -\nabla\Phi_{IF} \quad (3.3a)$$

$$\nabla^2\Phi_{IF} = 0 \quad (3.3b)$$

This interconnection potential Φ_{IF} satisfies the boundary condition:

$$-\frac{\partial\Phi_{IF}}{\partial n} = B_n \quad (3.4)$$

where B_n the normal component at the magnetopause. The distribution of normal components is calculated via the equation:

$$\nabla \times (\mathbf{v} \times \mathbf{B}_n) = 0 \quad (3.5)$$

which follows from the requirement that the tangential electric field across the magnetopause be curl-free:

$$\text{curl}(\mathbf{E}_t) = -\frac{\partial\mathbf{B}_n}{\partial t} = 0 \quad (3.6)$$

In equation (3.5) \mathbf{v} is the tangential component of the vector sum of the gasdynamic flow, which is obtained by the Spreiter-Stahara code (1980), and a merging outflow of open field lines –generally of the order of the local Alfvén speed-- which is appropriately inserted into the model. Following (3.5), a unique solution for the normal component everywhere in the magnetopause can be achieved when the normal component is specified along a boundary crossed by all field lines in time. After testing, Toffoletto and Hill selected the hemisphere/cylinder edge as this boundary. The resulting functional dependence of the normal component and of the associated interconnection field

everywhere at the magnetopause are described in detail by Toffoletto and Hill (1989; 1993). In this way the TH93 model achieves penetration of the IMF into the Earth's magnetosphere, a process controlled by the distribution of the magnetic normal component at the magnetopause.

To apply the TH93 model in Mercury, a number of modifications were performed. The dipole moment ($\sim 350 \text{ nT} \cdot R_M^3$) and radius ($R_M = 2,439 \text{ km}$) of Mercury were hardwired into the code, while the tilt of the dipole was set to zero degrees. In the absence of an energetic inner magnetosphere population the ring current was set to zero, while the near tail x-line was positioned at $2R_M$. Finally, the amount of the IMF penetration, which is the most important free parameter of the model, was set to 40% for a straight southward IMF ($\phi_{IMF} = 0$) at perihelion ($B_{IMF} = 46 \text{ nT}$) to reflect the increased reconnection at Mercury (Slavin and Holtzer, 1979). For all other solar wind and IMF configurations, the model computes this penetration factor as:

$$factor = 0.4 \times \frac{v_{sw} (km/s)}{430} \times \frac{B_{IMF} (nT)}{46} \times \cos^2\left(\frac{\phi_{IMF}}{2}\right) \quad (3.7)$$

These choices arise from the current state of our knowledge about the Hermean magnetosphere as was outlined in Chapter 2 of this work.

3.3 The Ding potential solver

Calculating the electric potential on magnetically open field lines is straightforward: open field lines, which are assumed to be equipotentials, map to the solar wind

$$\mathbf{E}_{SW} = -\mathbf{v} \times \mathbf{B}_{SW} \quad (3.8)$$

However, computing the electric potential along closed field lines of the magnetosphere requires a different approach.

The Ding (1995) potential solver extends the applicability of the TH93 open magnetosphere model to the closed line region. To map the electric field on closed field lines, this module employs finite element techniques to solve a 2-D Laplace equation for the electric potential:

$$\frac{\partial^2 \Phi}{\partial x^2} + \frac{\partial^2 \Phi}{\partial y^2} = 0 \quad (3.9)$$

under two boundary conditions: a) the distribution of the electric potential along the open-closed boundary; and b) the potential at the equatorward boundary. The latter is assumed to be zero, while the former is computed via the TH93 model.

Equation (3.9) is a simplified form for the current along a magnetic field line:

$$\nabla_{\perp} \cdot (\Sigma \nabla_{\perp} \Phi) = j_{\parallel} \quad (3.10)$$

where j_{\parallel} the field-aligned current and Σ the perpendicular height-integrated conductivity tensor. Assuming no field-aligned currents in the domain of the solution (the area between the open-closed and the equatorward boundaries), and that the conductivity tensor be uniform and anti-symmetric, equation (3.10) reverts to equation (3.9) which is solved by the Ding solver (Ding, 1995).

Programmatically, the code first computes the location of the open-closed boundary for given solar wind and IMF conditions. Second, it computes the electric potential along this boundary. Third, it extrapolates the potential distribution everywhere in the polar cap. Finally, the module solves equation (3.9) numerically in the closed field line area. In practice, the Ding (1995) solver provides the potential on a grid of 16x61 irregularly spaced points on each hemisphere that lie on either open and on closed field lines. In this

way, the Ding potential solver provides the electric potential everywhere in the ionosphere or, in Mercury's case, on the surface.

When the electric potential is asked at any point (x, y, z) of the magnetosphere, the model traces a magnetic field line from that point to the surface (x_0, y_0, z_0) . Because it is assumed that magnetic field lines are equipotentials, the potential $\Phi(x, y, z)$ equals the potential $\Phi(x_0, y_0, z_0)$, which can be interpolated from the gridded data computed by the solver. Since the electric field equals the gradient of the electric potential, the electric field vectors are computed by applying the finite difference method ("centered differencing"). For example, the x-component:

$$E_x(x, y, z) = - \left(\frac{\Phi(x + \Delta x) - \Phi(x - \Delta x)}{2 \bullet \Delta x} \right) \quad (3.11)$$

As magnetic and electric field grids are sampled every $0.1 \cdot R_M$ in this work, typically $\Delta x = 0.05 \cdot R_M$.

Only two modifications are needed to apply the Ding potential solver to Mercury: estimating a realistic maximum polar cap potential drop and specifying the location of the equatorward boundary at Mercury.

The estimated potential drop across the dayside magnetosphere (with a diameter of $3.5 R_M$) at perihelion (where $B_{sw} \sim 46$ nT) is:

$$\Phi_{SW} \sim v_{SW} \cdot B_{SW} \cdot (3.5 R_M) \sim (400 \text{ km/s})(46 \text{ nT})(3.5 \cdot 2.439 \cdot 10^3 \text{ km}) \sim 157 \text{ kV} \quad (3.12)$$

Assuming 40% penetration of the electric field for a straight southward IMF at perihelion gives a polar cap potential drop at perihelion:

$$\Phi_{PC}^{PER} \approx 0.4 \cdot (157 \text{ kV}) \approx 60 \text{ kV} \quad (3.13)$$

The potential solver then normalizes the polar cap potential drop for every other configuration as:

$$\Delta\Phi_{PC} = 60kV \cdot \frac{B_{IMF}(nT)}{46} \cdot \sin^3\left(\frac{\theta}{2}\right) \quad (3.14)$$

where $\theta = \cos^{-1}\left(\frac{B_z}{B}\right)$ (Reiff and Luhmann, 1986).

The second modification involves the location of the equatorward boundary. In the Earth-based model, the potential solver approximates the equatorial boundary as a constant-latitude circle whose location is a function of the polar cap potential drop:

$$g_{lat} = \frac{180}{\pi \cos^{-1}(1/\sqrt{R_B})} \quad (3.15)$$

with $R_B \propto \Delta\Phi_{PC}^{-1/2}$ (Ding, 1995).

Because of the expected absence of low-latitude field-aligned currents at Mercury, which follows the nil ring current, we set the equatorial boundary to zero degrees, i.e. the equator. Since the potential solver provides the potential along closed field lines in a domain where there are no field-aligned currents, it is now applicable to the entire magnetosphere of Mercury.

3.4 The particle tracer

The full-particle tracer we employ in this thesis includes the gravitational force:

$$\frac{d^2\mathbf{v}}{dt^2} = \frac{q}{m}(\mathbf{v} \times \mathbf{B} + \mathbf{E}) + \frac{\mathbf{F}_{grav}}{m} \quad (3.16)$$

$$\mathbf{v} = \frac{d\mathbf{r}}{dt} \quad (3.17)$$

These equations are solved for each particle using the MATLAB ode23 function, with an adaptive timestep, and absolute and relative tolerances of 10^{-7} and 10^{-4} , respectively, given an initial position and velocity. As input to the particle tracing code we produce a 3-d grid of magnetic and electric fields at Mercury sampled every $0.1 R_M$. Testing showed that, while photoion trajectories are not critically affected by this choice of grid step, crossings of the magnetopause by solar wind ions requires a finer grid of $0.05 R_M$. At any point along a particle's trajectory, the fields are calculated with 3-d interpolation from the edges of the (cubic) volume of the grid where the particle lies at the time.

3.5 Computing solar wind particle fluxes: the Onsager method

In order to predict the solar wind particle flux that impacts Mercury's surface under various solar wind and IMF conditions, this work draws on a scheme first implemented by Onsager et al. (1993; 1995). This method consists of three steps: first, we follow particle trajectories upwards and backwards in time from spacecraft locations in the Earth's ionosphere where they are detected to locations in the magnetopause where these particles crossed; there, we account for the acceleration or deceleration of particles when they crossed the magnetopause current sheet; and, last, we obtain particle space densities at these spacecraft locations from magnetosheath ion distribution functions assuming that, according to Liouville's theorem, particle phase space densities are conserved along particle trajectories. While Onsager used simplistic approximations for the magnetospheric electric field, this process was expanded by Xue (1996) to successfully

incorporate the Onsager method with self-consistent magnetic and electric fields given by the TH93 and Ding (1995) models. This thesis extends their cusp particle injection model to the entire dayside of Mercury, launching particles from both high and low latitude locations of the Hermean surface.

In step 1, solar wind protons (with a range of energies and pitch angles) are launched from regularly spaced locations on Mercury's surface towards the magnetopause. Particles with small energy $\mathbf{E} \times \mathbf{B}$ drift farther, so they cross the magnetopause closer to the reconnection site (velocity-filter effect). When a particle crosses the (inner) magnetopause, we record the location of impact (x_{mp} , y_{mp} , z_{mp}) and the velocity components $v_{||}$, v_{\perp} .

In step 2, we reconstruct the particle velocities on the outer edge of the magnetopause from their velocities in the inner magnetopause, which were computed in step 1. To this end, we specify for each particle a local de Hoffman-Teller (HT) frame that moves along the magnetopause at speed:

$$\mathbf{V}_{HT} = \mathbf{E}_T \times \mathbf{B}_N / B_N^2 \quad (3.18)$$

where \mathbf{E}_T the tangential electric field and \mathbf{B}_N the normal component at the local magnetopause (Cowley, 1995).

To evaluate the particle flux in the final step, we assume, after Hill and Reiff (1977), that ions at the outer magnetopause are distributed according to the bi-Maxwellian phase space density

$$f(\mathbf{V}) = n \left(\frac{m}{2\pi K T_{||}} \right)^{\frac{1}{2}} \left(\frac{m}{2\pi K T_{\perp}} \right) \exp \left[-\frac{m(V_z - V_{||})^2}{2K T_{||}} - \frac{m V_{\perp}^2}{2K T_{\perp}} \right] \quad (3.19)$$

where n and m are the number density at the magnetopause and mass of solar wind protons, respectively; KT_{\parallel} and KT_{\perp} the solar wind thermal energies parallel and perpendicular to the magnetic field; V_z the magnetosheath field-aligned plasma bulk flow, and V_{\parallel} and V_{\perp} the particle's velocity in the magnetosheath. For an isotropic plasma in the magnetosheath, $T_{\parallel} = T_{\perp} = T/2$.

The magnetosheath plasma density and temperature are determined as polynomial fits derived from the gasdynamic code of Spreiter-Stahara. We used a fit for Mercury provided by Masetti et al (2003) as follows:

$$\frac{n}{n_{SW}} = 3.3 - 3.22d + 1.4d^{1.5} \quad (3.20)$$

$$\frac{T}{T_{SW}} = 1 + 3(1 - (-0.249d + 0.953d^{1/2})^2) \quad (3.21)$$

where $d = d_{\text{nose}} - x_{\text{mp}}$ the distance from the subsolar point to the point where the particles crossed the magnetopause.

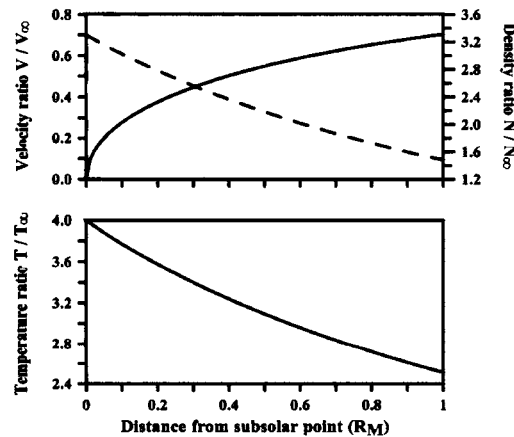


Figure 3.1: Variation of Mercury's magnetosheath density and temperature that was used to compute solar wind particle fluxes in this work. (After Masetti et al, 2003)

To calculate the term $V_z - V_{\parallel}$, we follow Xue (1996):

$$V_z - V_{\parallel} = V_{\parallel}^{HT} - V_A \quad (3.22)$$

where $V_{\parallel}^{HT} = V_{\parallel} - V_{HT,\parallel}$ the parallel velocity of the particle in the HT frame,

$V_{HT,\parallel} = \mathbf{V}_{HT} \cdot \hat{b}_{mag}$ the projection of the de Hoffman – Teller velocity to the (inner)

magnetic field, and V_A the Alfven velocity. Eqn (3.19) then yields:

$$f(\mathbf{V}) = n \left(\frac{m}{\pi KT} \right)^{\frac{3}{2}} \exp \left[-\frac{m(V_{\parallel}^{HT} - V_A)^2}{KT} - \frac{mV_{\perp}^2}{KT} \right] \quad (3.23)$$

The differential particle flux is then computed as:

$$J = \left(\frac{2E^2}{m^2} \right) f(\mathbf{V}) \quad (3.24)$$

where E and m the energy and mass, respectively, of the tracked particle.

3.6 Limitations of the application of the TH93 model at Mercury

Since the location of the magnetopause critically affects computations of solar wind particle flux that impacts Mercury's surface, the most significant approximation that our model makes is its fitting of a prescribed magnetopause. What is required is an accurate computation of magnetopause location, specifically of the magnetopause subsolar distance. While testing a range of dipole moments between 300-400 nT R_M^3 did not significantly affect the location of the magnetopause, other parameters (e.g., compressibility) may be variable at Mercury as the magnetopause gets pushed close to

the surface. Induction currents, which are not included in our model, may also prevent significant erosion of the dayside magnetopause.

In all other aspects we stayed within the model's solution domain. For example, while the IMF penetration was normalized to 40%, the scaled penetration factor given by equation (3.7) was about 20-30% in modeled cases of this work; note that the Earth-based model has successfully shown to reproduce the magnetospheric configuration of the Earth for southward IMF when about 20% penetration of the IMF is expected.

There are critical issues regarding the applicability of any model of the Earth's magnetosphere to Mercury. For example, some analytic models (e.g., Luhmann et al., 1998; Delcourt et al., 2002; 2003; Massetti et al., 2003) use scaling of an Earth-based model to simulate the solar wind-Hermean magnetosphere interaction. This scaling factor is calculated using a simple pressure balance equation that includes the radii and dipole moments of Mercury and the Earth, as well as the solar wind velocity and IMF magnitude at the locations of the two planets. When the solar wind velocity is not the same at the two locations, i.e. during a directional CME event that crosses Mercury but misses the Earth, or when the IMF at Mercury is not a nominal Parker field, the validity of this approach breaks down. As a second point, these models do not include the B_x component which is dominant at Mercury. In addition, MHD models (Kabin et al., 2000; Ip and Kopp, 2002) may not be as successful at Mercury as they are at the Earth. Two assumptions of MHD models are invalid at Mercury: the existence of a thin shock boundary and the assumption of thermal equilibrium. While the gyroradii of heavy ions can be as large as one planetary radius at Mercury, which invalidates the assumptions of a thin shock boundary and collective ion behavior, the Mariner 10 spacecraft measured a

non-thermal electron distribution (Christon, 1987), which invalidates the assumption of thermal equilibrium.

Even though we avoid scaling issues in TH93 by hardwiring Mercury's dipole moment and radius, this work did not introduce any new, Mercury-specific physics to the Earth-based TH93 model. New missions to Mercury that are either being planned (ESA's Bepi/Colombo) or have already been launched (NASA/MESSENGER) will provide invaluable new knowledge that will enable the magnetospheric community to build accurate models of energy transport in Mercury's magnetosphere. Until then, the modified TH93 model presented in this work can successfully be used either as a tool for mission planning and as a tool of analysis for upcoming mission data.

CHAPTER 4:

PHOTOION TRACINGS

4.1 Objectives

This chapter presents new tracings of magnetospheric ions (Na and K) in Mercury's magnetosphere that model the variability of the sodium and potassium ion surface fluxes in Mercury. We capitalized on a new analysis of the Helios I and II data for times when the spacecrafts were at appropriate orbital distance and heliospheric latitude for Mercury (Killen, personal communication). In agreement with this analysis, three solar wind and interplanetary magnetic field (IMF) configurations are tested: two cases with a dominant radial (B_x) component (aphelion vs perihelion), and one aphelion case with a dominant southward B_z component. The reason behind testing two aphelion cases lie in the imaging data of November 13-20, 1997, which we are trying to explain: at that time, Mercury was at 0.44 AU, very close to its aphelion.

We computed the flux of sodium and potassium ions that impacts Mercury's surface under these conditions. Results are analyzed to evaluate the relative importance of ion sputtering as a source mechanism for Mercury's atmosphere, as well as to understand the variability of the Na/K ratio in the atmosphere of Mercury.

4.2 Choices of particles and fields: implications of the Helios I and II datasets for the long-term variability in the environment of Mercury

In the absence of a large body of *in situ* measurements of Mercury's particle and field environment, appropriate input has hindered modeling efforts so far. For instance, although the IMF radial component (B_x) is believed to be dominant at Mercury, some authors argue that they "expect the IMF at the orbit of Mercury to be characterized by strong deviation from the nominal Parker spiral, especially during periods of high solar activity" (Masetti et al., 2003), and accordingly ignore the effects of the IMF B_x (e.g., Luhmann et al., 1998; Delcourt et al., 2002; 2003; Masetti et al., 2003). In such B_x -free models it is required that high values of southward IMF B_z be applied to the magnetosphere to produce a realistically open configuration. Specifically, Masetti compared cases with IMF B_z ranging between -10 nT and -30 nT, while Delcourt used a $B_z = -30$ nT for his sodium photoion tracings. How often these conditions are met is a matter of speculation. Therefore, a more systematic assessment of the solar wind and IMF input is clearly needed before we run additional cases.

To test how often the radial component of the IMF is dominant, we analyzed the Helios I and II magnetic field data collected while the spacecraft were at Mercury's orbital range and heliospheric latitude, which happened for about 14,000 hours of observations. To this end, we used hourly averages of the IMF and defined a dominant B_x as one being at least twice as much as any of the other two components. Preliminary results by Killen show that the B_x was "dominant" according to the above definition

between 32-57% of all time (Figure 4.1): each set of data is defined as one spacecraft pass between 0.31 AU to 0.47 AU. The lowest occurrence of a dominant Bx in a set was 32%, while the highest was 57%. On the average, Bx was dominant about 45% of the total time in Helios I and II data. The cases investigated in this thesis reflect this important result.

Unlike the fields used by Delcourt et al. (2003), who applied a 30 nT field straight southward for his photoion tracings, the IMF in Helios I and II is rarely observed to be more negative than -10 nT, and even more rarely is found to be both southward and stronger than the radial Bx. As Table 4.1 asserts, the former happens on the average 11% of the total observation time, while the latter condition is met for about 7% of the time.

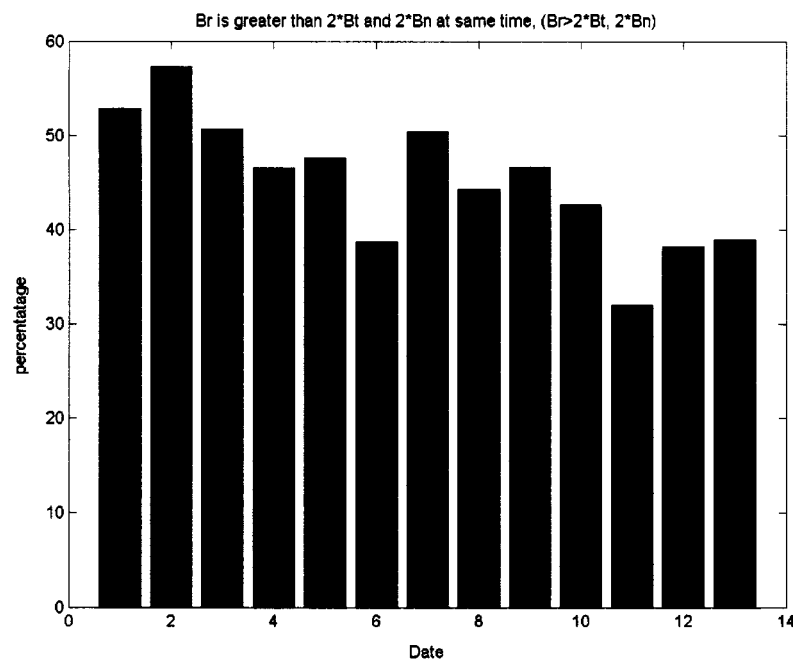


Figure 4.1: Helios I cumulative data confirming that the IMF Bx is frequently dominant at Mercury. (Killen, personal communication)

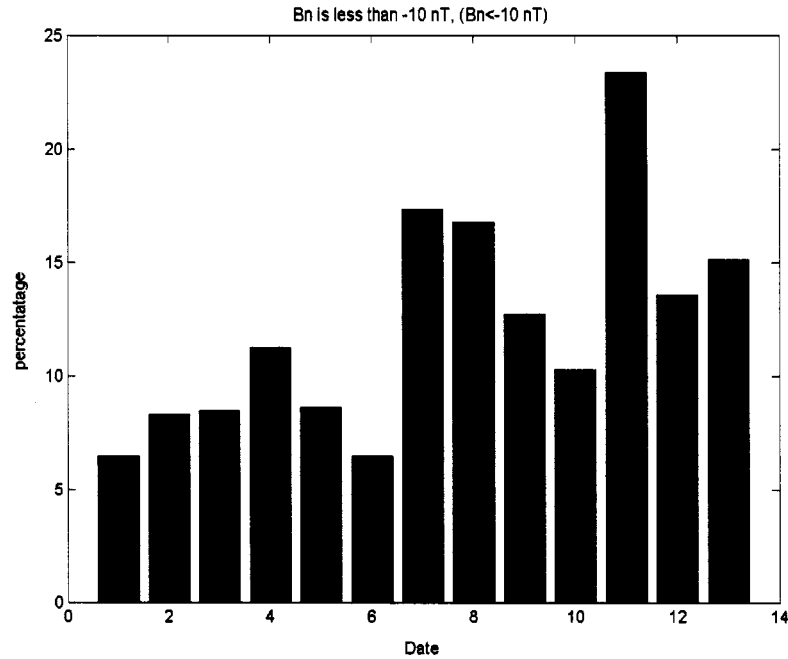


Figure 4.2: The Helios I record for Mercury shows that Bz is rarely more southward than -10 nT, conditions that were used in setups of other models of Mercury's magnetosphere. (Killen, personal communication)

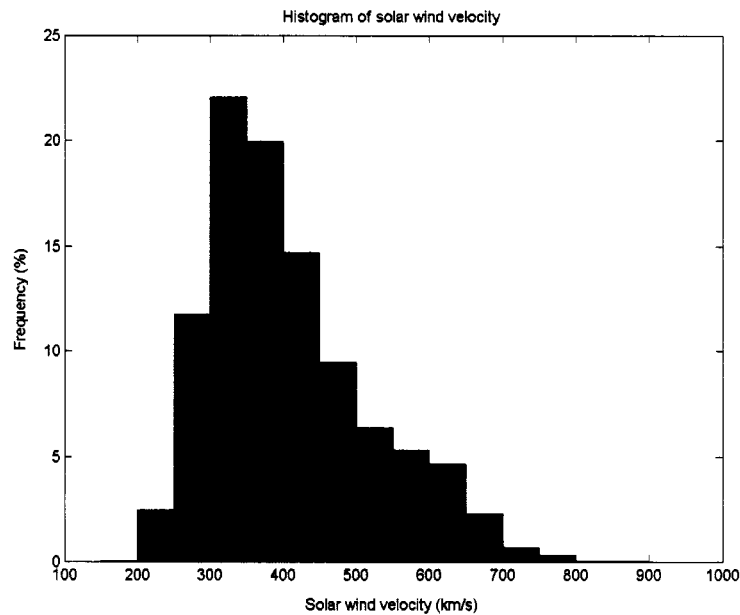


Figure 4.3: The solar wind at Mercury as observed by the Helios I spacecraft. Conditions were nominal, with high speed streams occurring, on the average, for just seven percent of time. (Killen, personal communication)

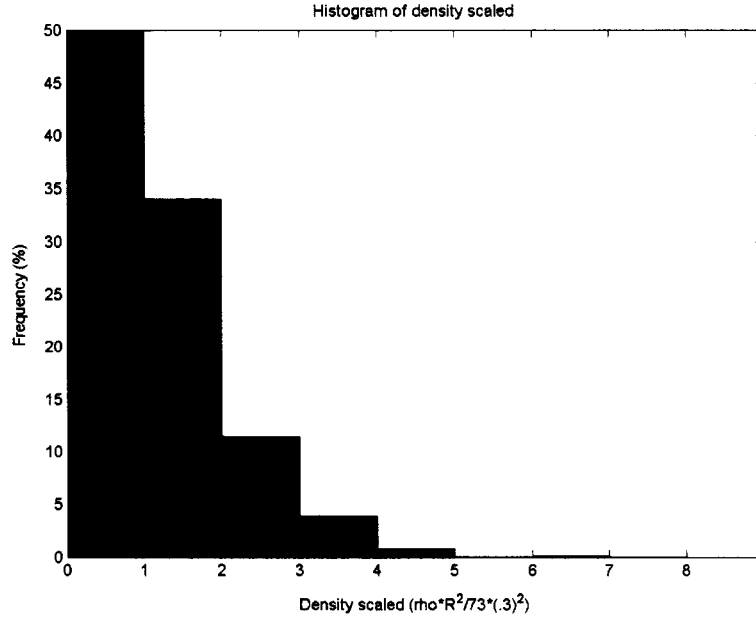


Figure 4.4: When the solar wind density observed by Helios I is compared to the nominal Parker density at each location, it is found that half the time the observed density is higher than the nominal value (Killen, personal communication).

Clearly the configurations for Masetti et al. (2003), testing solar proton precipitation, and for Delcourt et al. (2003), testing sodium ion recycling, are unrealistic in the sense that they represent very transient events but not the most likely conditions at Mercury. In this thesis, we model one case with $B_z = -5$ nT, and two cases with $B_z = -10$ nT.

The solar wind density and velocity are two additional parameters required as input to our model. As figure 4.3 depicts, the solar wind observed by Helios I was nominal with high speed spurts (>600 km/s) that amounted to about 8% of all measurements. On the other hand, the measured density appeared to be stronger than the nominal scaled density $n \propto 1/R^2$ about half the time (Figure 4.4). The most important consequence of a high density is that the magnetopause standoff distance, which is calculated in our model, may

be pushed very close to the planet. When solar wind ion gyroradii become comparable to the magnetopause distance, significant penetration may happen along closed field lines. To give a realistic prediction for the extent of this precipitation along closed field lines in the next chapter, we tried one perihelion case with $n_{sw} = 73 \text{ cm}^{-3}$ and $v_{sw} = 430 \text{ km/s}$. In contrast, our aphelion cases used $n_{sw} = 32 \text{ cm}^{-3}$ and $v_{sw} = 430 \text{ km/s}$.

Table 3.2 summarizes the test cases that were modeled in this work. At aphelion the magnitude of the magnetic field was set to a nominal 26 nT, while at perihelion we used a 46 nT field. The IMF was reduced to its components using a 20-degree Parker spiral angle at perihelion, and was scaled to aphelion conditions as $1/R^2$ for Bx and $1/R$ for each of By and Bz.

	Helios 1	Helios 2
Dominant Bx	46.0%	43.3%
Bz < -10 nT	11.7%	11.6%
Bz < 0 and $ Bz > Bx $	6.7%	6.6%
$V_{sw} > 600 \text{ km s}^{-1}$	8.8%	7.9%
$N_{sw} > N_{nominal}$	44.6%	50.1%

Table 3.1: Averaged conditions for Mercury derived from the Helios I and II data while the spacecraft were at Mercury’s orbital range and heliospheric latitude (Killen, personal communication). These conclusions, namely that the IMF Bx is very often dominant while the IMF Bz is rarely less than -10 nT , were used for the setup of our modeling runs. The observed solar wind velocity was nominal, but the solar wind density was often stronger than the local density predicted by the Parker model.

IMF[Bx,By,Bz](nT)	V_{sw} (km s ⁻¹)	N_{sw} (cm ⁻³)	Case
[-43,10, -10]	430	73	perihelion
[-19, 5, -5]	430	32	Aphelion, weak Bz
[-10, 5, -10]	430	32	Aphelion, strong Bz

Table 3.2: Summary of solar wind and IMF input for (global) cases examined in this work. At aphelion the magnitude of the magnetic field was set to a nominal 26 nT, while at perihelion we used a 46 nT field. The IMF was reduced to its components using a 20-degree Parker spiral angle at perihelion, and was scaled to aphelion conditions as $1/R^2$ for Bx and $1/R$ for each of By and Bz.

4.3 Tracings of magnetic field lines with the TH93 model

In Figures 4.5, 4.6, and 4.7 we present the structure of the Hermean magnetosphere obtained by the modified TH93 model for the three scenarios of this work. Magnetic field lines were traced every two degrees of latitude from the ionosphere in the noon-midnight plane ($Y_{GSM} = 0$). These plots demonstrate that Mercury's magnetospheric configuration responds to changes in the solar wind dynamic pressure and the IMF. A strong Bx controls which hemisphere is more open, while Bz regulates the latitude of the open field lines as well as the size of the cusps. We found that, when the IMF Bx is

strong ($B_x \gg |B_z|$), field lines turn towards the solar wind in one hemisphere and away from it in the other, but when B_z becomes comparable to B_x , this north-south asymmetry in the direction of open field lines grows less pronounced. Solar wind ions are more likely to impact the surface along lines directed sunwards because, in this case, they have a more direct path along the magnetic field. Thus, the fluxes are larger in the southern hemisphere for $B_x > 0$, and vice versa.

A significant improvement of field line tracings in this work stems from an improved distribution of the normal component: while in earlier results open magnetic field lines were dragged past the planet before turning towards the solar wind, these new configurations look more realistic, with a lot more reconnection on the dayside, and result in higher impact fluxes for the solar wind. (Compare, for example, figs 4.7 and 4.8.)

Case	Magnetopause nose distance (R_M)	Polar cap potential drop (kV)
Perihelion	1.12	24.0
Aphelion, weak B_z	1.34	11.3
Aphelion, strong B_z	1.22	12.9

Table 3.3: Computed magnetopause standoff distance and polar cap potential drop for modeled cases of this work.

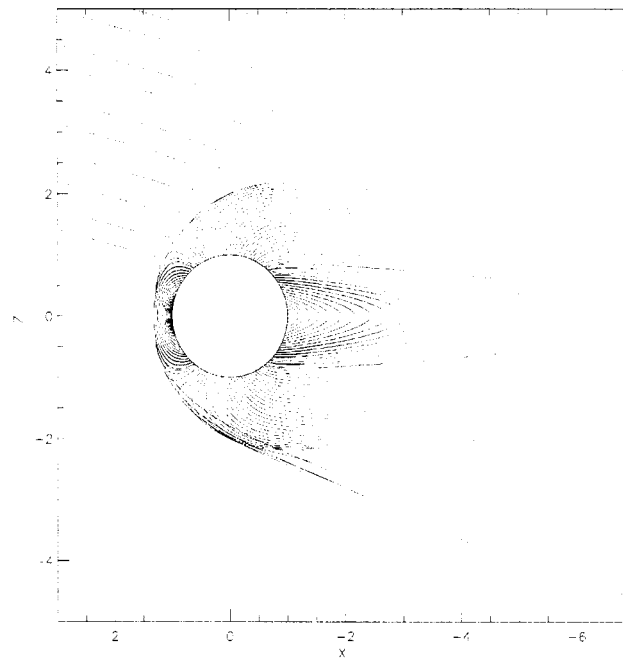


Figure 4.4: The noon-midnight meridian plane configuration of Mercury's magnetosphere for IMF $(B_x, B_y, B_z) = (-19, 5, -5)$ nT at aphelion ("weak B_z "). The x-axis is pointing towards the Sun.

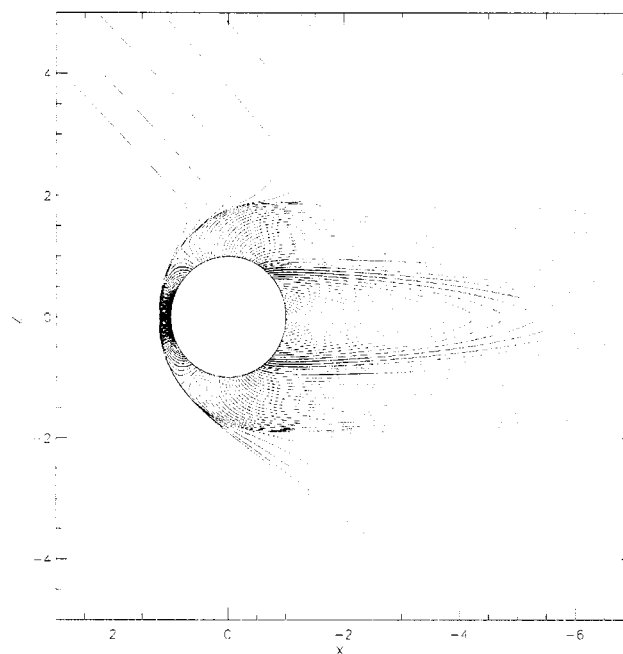


Figure 4.5: The noon-midnight meridian plane configuration of Mercury's magnetosphere for IMF $(B_x, B_y, B_z) = (-10, 5, -10)$ nT at aphelion ("strong B_z ").

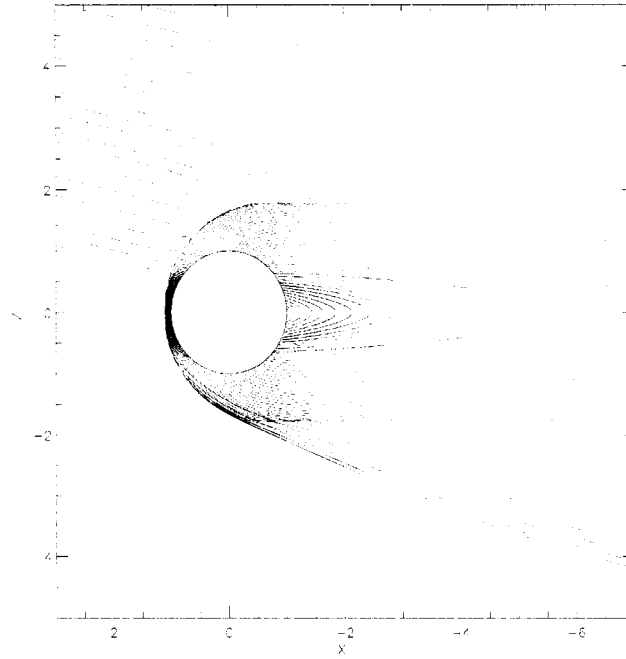


Figure 4.7: The noon-midnight meridian plane configuration of Mercury's magnetosphere at perihelion for IMF $(B_x, B_y, B_z) = (-43, 10, -10)$ nT.

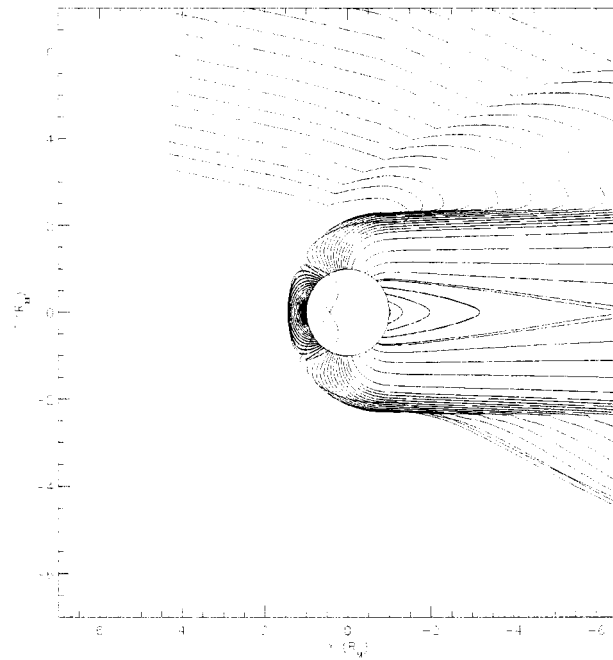


Figure 4.8: In earlier setups of the TH93 model for Mercury, all open field lines were dragged towards the tail before crossing the magnetopause. This configuration, run for IMF $[-25, 5, -5]$, would produce reduced impact fluxes (Sarantos et al., 2001).

In agreement with expectations, the subsolar magnetopause distance was found to be very close to the planet. At perihelion, especially, the magnetopause is just $0.12 R_M$ above the surface of Mercury. Since the solar wind Larmor radius becomes comparable to the magnetopause distance under these conditions, we will use this configuration to test how much of the total flux impacts the surface along closed field lines.

The pronounced stretching of the tail field, which is illustrated in these plots, gives rise to so called “Speiser orbits” very close to the planet as we will demonstrate in the next paragraph.

4.4 Model photoion trajectories

In this application we launched individual particles from mid and high latitudes (45° - 75°) of the dusk sector from an altitude of 1 km above the surface, and mapped their trajectories given an exploratory IMF. Most duskside ions are swept away by the solar wind down the tail or through the magnetopause flank, but some particles go down the tail, turn around, execute Speiser orbits in the tail current sheet, and impact the nightside at $\sim 10\text{keV}$ producing ion sputtering or implantation. Speiser orbits, which exhibit a fast oscillation in the z-direction but a slow gyromotion around the normal magnetic field, typically arise at distances farther than about $10R_E$ in the Earth’s magnetotail. At Mercury, however, because even field lines that are very close to the planet are stretched as indicated in Figs 4.5 – 4.7, these trajectories occur much closer to the planetary surface. A comparison between the sodium and potassium ions in Speiser orbits shows that, while sodium ions turn around at about $1 R_M$ down the tail, potassium ions travel

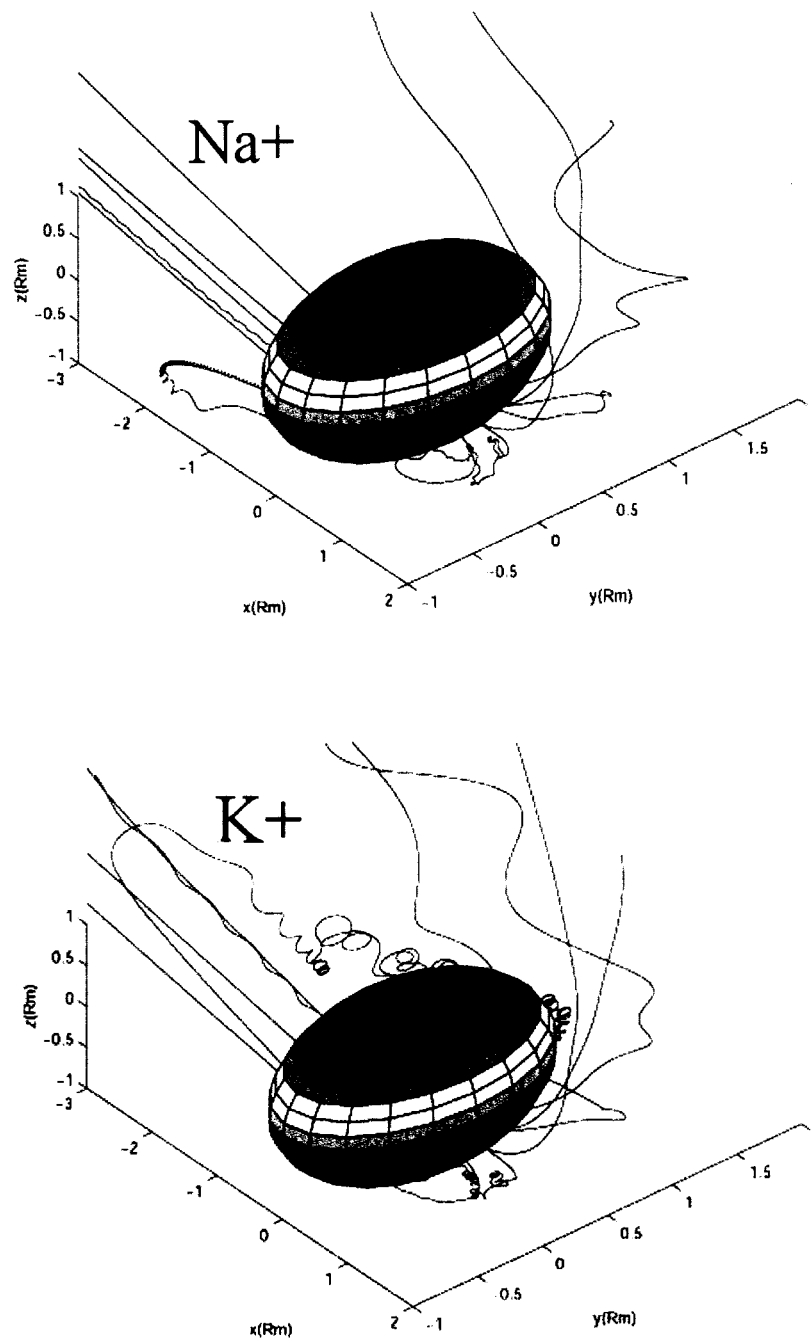


Figure 4.9: Sample of sodium (upper pannel) and potassium (lower pannel) photoion trajectories in Mercury's magnetosphere. Duskside potassium ions were released from the southern hemisphere at 45, 60 and 75 degrees latitude. The Sun, in this picture, lies in the positive X-direction. The IMF was set to [20, -10, -10] nT, while the magnetopause radius was 1.50 Rm.

farther down they tail before doing so, thus risking escape to the solar wind. From this argument, we predict fewer energetic hits in the nightside for potassium than for sodium ions.

Residence times for these photoions are fairly short with the exception of Speiser-type orbits: we compute that it takes about ten seconds for an emitted ion to recycle to the surface of the planet, thirty seconds to a minute to escape to the solar wind, but up to 30 minutes when it gets trapped in the tail current sheet. These residence times generally agree with those by Delcourt et al. (2003) except for the Speiser orbits, which take 10 minutes in their model but 30 minutes in ours.

4.5 Photoion fractional recycling and escape to the solar wind

Earlier results from the model of this work were obtained by launching particles from the surface or just a few kilometers above it. High recycling rates (~60%) and a (times four) asymmetry in dawn-dusk recycling were reported (e.g., Killen et al., 2003; 2004).

But a quick calculation reveals that the fraction of atoms below a given height, h , in Mercury's exosphere is:

$$1 - \exp(-h/H) \quad (4.1)$$

where h is the height and H is the scale height (112 km for Na; 88 km for K at the subsolar point). Since Mercury's exosphere is optically thin, roughly 99% of all photoionization events occur above 1 km, but only 37% of photoions are created above the scale height. More importantly, because the Hermean atmosphere is not accommodated to the surface temperature, the scale height for each species probably

remains the same throughout Mercury's orbital distances. This fact allows us to track changes in photoion recycling and escape due only to changes in the magnetosphere, launching particles from a single shell representative of all photoionization (the scale height), with minimal computational time cost.

In the global simulations presented here, about 1,000 ions of either species are followed in a tight grid of magnetic and electric fields at Mercury for each of our three scenarios. The ions are launched at the scale height, with an isotropic angular distribution with respect to the vertical at each launching site, every 15 degrees of latitude and 30 degrees of longitude to cover the entire dayside. Because neutrals with energy higher than 2 eV escape, the initial ion energy is taken to be 1eV. Ions are tracked until they either hit the surface of the planet, crossed the magnetopause, or reached 4 R_m down the tail, where they are considered to have escaped to the solar wind.

While we principally present results for an isotropic atmosphere in this work, we also used a different functional dependence of the initial ion distribution to simulate Mercury's atmosphere at quiet time. In the absence of significant ion sputtering, when the entire atmosphere is driven by photon-stimulated desorption, we let the initial ion spatial distribution vary as $F_{SUB} \cos^{1/2} \phi \cos^{1/2} \vartheta$, where ϕ and θ are the launching latitude and longitude measured from the subsolar point.

4.5.1 Sodium and potassium global runs

In these simulations ions can do one of two things: escape to the solar wind, or impact the surface. But what fraction of magnetospheric ions escape to the solar wind, and what

impacts the surface? When ions impact at high energy, they either cause sputtering or they are implanted deep into the grains, where they enhance radiative diffusion from the grains. Previous studies have suggested that bombardment of the surface by energetic magnetospheric ions may enhance the content of the atmosphere. Heavy ions, such as Na^+ and K^+ , are very efficient sputterers with yields of about 0.1 per incident particle. But if they impact at low energies (generally less than 300 eV), they adsorb, or loosely stick to the surface, and can be easily reexcited (Dukes and Baragiola, 2002) thus raising the total atmosphere content. In this section we determine whether the fraction of particles that escape to the solar wind is variable, and whether impacts dominate.

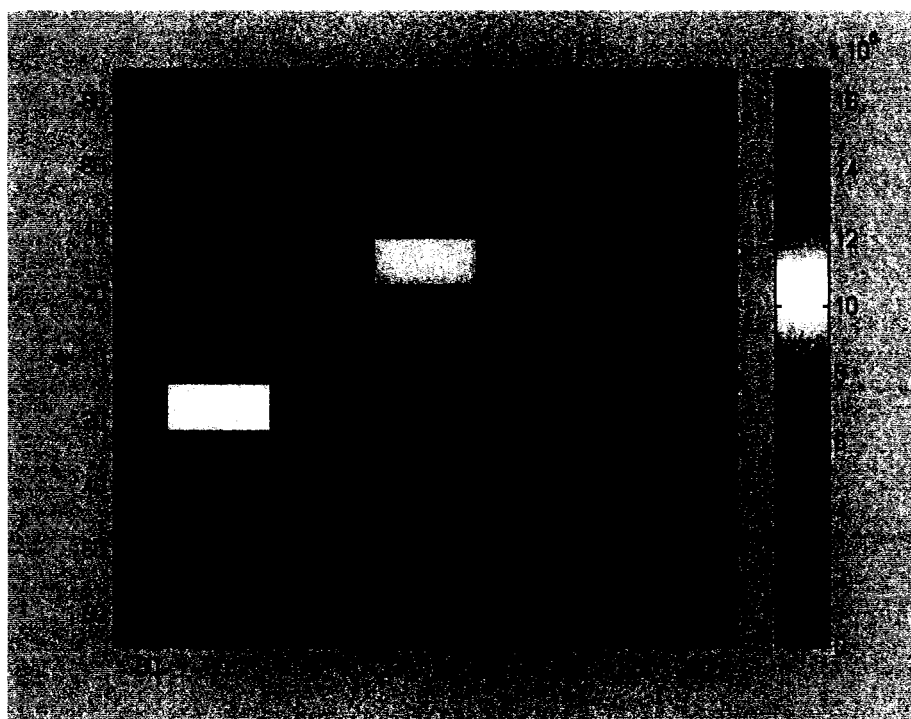


Figure 4.10: Map of dayside Na^+ precipitation for the IMF case $[-43, 10, -10]$ at perihelion. Shown is the color-coded ion flux ($\text{cm}^{-2} \text{s}^{-1}$) in the case of an isotropic atmosphere. In this figure north is down, while dawn is at left.

But we must differentiate between counts that return to the dayside vs to the nightside: due to the very slow rotation of the planet with respect to the Sun ($\sim 2^0$ per day), nightside neutrals would be unavailable for quite some time, unlike dayside ions that neutralize within a few seconds after impact, and are available to be released almost immediately. Therefore, we track dayside and nightside impacts separately in this section.

To compute the sodium photoion flux at aphelion, we used an average sodium column abundance of $2 \times 10^{11} \text{ cm}^{-2}$ ($1 \times 10^{11} \text{ cm}^{-2}$ at perihelion), while the photoionization lifetime is given as $1.6 \times 10^5 R^2 \text{ (AU)}$ (Huebner et al, 1992).

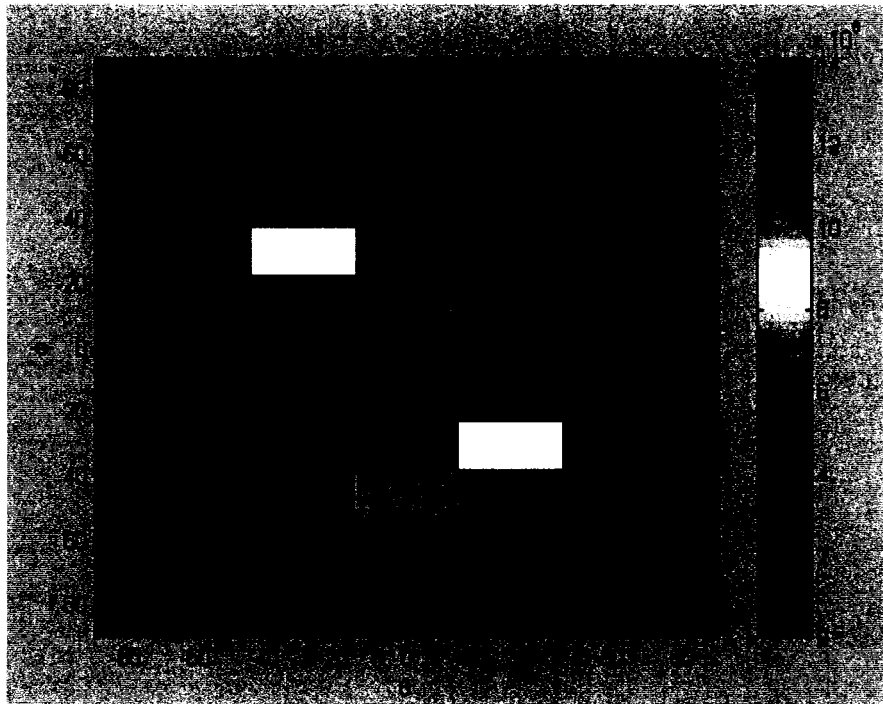


Figure 4.11: Map of the dayside Na^+ precipitation flux ($\text{cm}^{-2} \text{ s}^{-1}$) for an isotropic atmosphere at aphelion with IMF [-19, 5, -5]. Note that North is down in this figure, while dawn is at left.

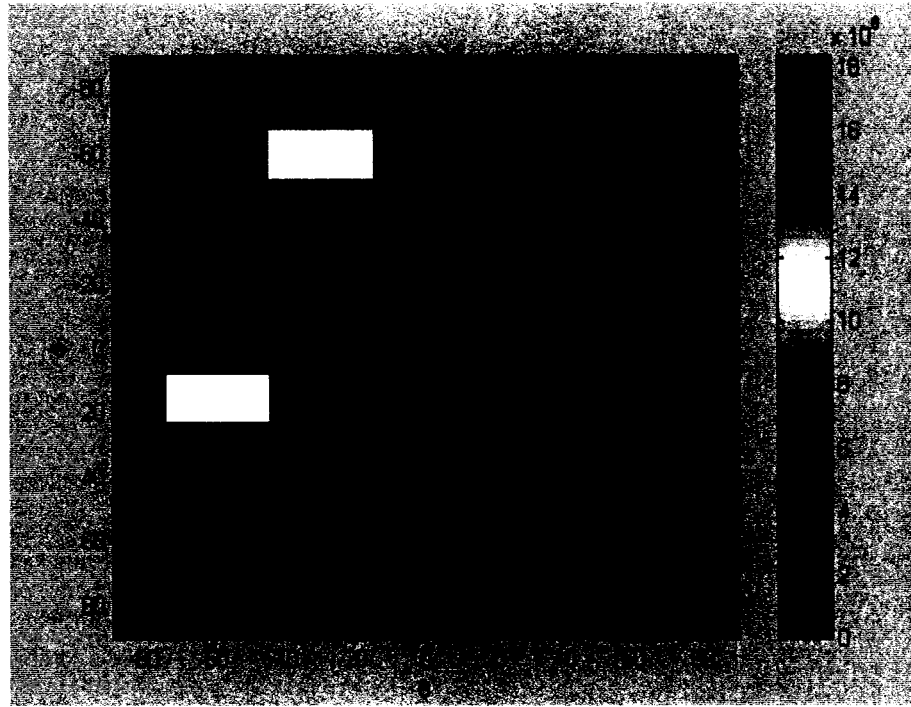


Figure 4.12: Na^+ precipitation flux ($\text{cm}^{-2} \text{s}^{-1}$) for an isotropic atmosphere at aphelion case with IMF [-10, 5, -10].

This yields $6.5 \times 10^6 \text{ cm}^{-2} \text{s}^{-1}$ at perihelion, and $5.65 \times 10^6 \text{ cm}^{-2} \text{s}^{-1}$ at aphelion. The potassium photoion flux was computed assuming that, on the average, the potassium column is 100 times less, and that the photoionization rate for potassium is 1.5 faster than for sodium.

The ion redistribution patterns of this work, which are presented in Figs 4.10 – 4.16, do not confirm earlier reports of enhanced (times four) recycling efficiency in the dawnside when particles were launched from close to the surface. While dawnside ions may still predominantly recycle, their residence times are higher when they are launched from the scale height, and they **ExB** drift farther from their cell, populating the dusk sector. Our results indicate that, while at perihelion there are almost equal numbers of

Perihelion		
	Na^+	K^+
Global recycling (1)	62.1%	59.3%
Effective recycling (2)	45.6%	43.4%
Escape (3)	37.9%	40.7%
Sputtering (4)	16.5%	15.9%

Aphelion, weak Bz		
	Na^+	K^+
Global recycling (1)	70.9 %	71.7%
Effective recycling (2)	66.2%%	66.5%
Escape (3)	29.1 %	28.3%
Sputtering (4)	4.7%	5.2%

Aphelion, strong Bz		
	Na^+	K^+
Global recycling (1)	68.1%	68.7%
Effective recycling (2)	57.6%	58.8%
Escape (3)	31.9%	31.3%
Sputtering (4)	10.5%	9.9%

Table 3.4: Fractional percentage of Na^+ and K^+ particles that (1) returned to the surface; (2) returned with energies < 300 eV causing adsorption rather than sputtering or implantation; (3) escaped to the solar wind; and (4) caused sputtering for our three configurations. While long-term recycling is very strong, it reduces by about a factor of 1.5 at perihelion. This could help explain why the sodium atmosphere is denser at aphelion. No statistical difference of the fractional escape rate of sodium and potassium ions was found, disproving the hypothesis that higher recycling for potassium is responsible for the variable Na/K ratio in the atmosphere.

Perihelion		
	Na^+	K^+
Dayside (DS) impacts (1)	37.9%	33.7%
Effective DS recycling (2)	25.3%	25.3%
Nightside impacts (3)	24.2%	25.6%
Sputtering on nightside (4)	3.9%	7.5%

Aphelion, weak Bz		
	Na^+	K^+
Dayside (DS) impacts (1)	46.4%	46.4%
Effective DS recycling (2)	42.9%	42.5%
Nightside impacts (3)	24.5%	2.8%
Sputtering on nightside	1.2%	1.2%

Aphelion, strong Bz		
	Na^+	K^+
Dayside impacts (1)	58.2%	57.7%
Effective DS recycling (2)	56.9%	57.1%
Nightside impacts (3)	9.9%	11.0%
Sputtering on nightside (4)	9.2%	9.3%

Table 3.5: Comparative sodium and potassium results for dayside vs nightside impacts. Tabulated are the fractions of total flux of Na and K ions that (1) returned to the dayside surface; (2) returned to the dayside with energies <300 eV causing adsorption rather than sputtering or implantation for our three configurations; (3) returned to the nightside; or (4) caused sputtering in the nightside. Significant high-energy impacts in the nightside, which are seen when Bz is strongly negative, can contribute to the observed sodium tail of Mercury.

particles impacting the dayside or nightside, at aphelion about two to four times as many ions are implanted on the dayside as those implanted on the nightside. Details about the fate of sodium and potassium ions are summarized in Tables 3.4, 3.5.

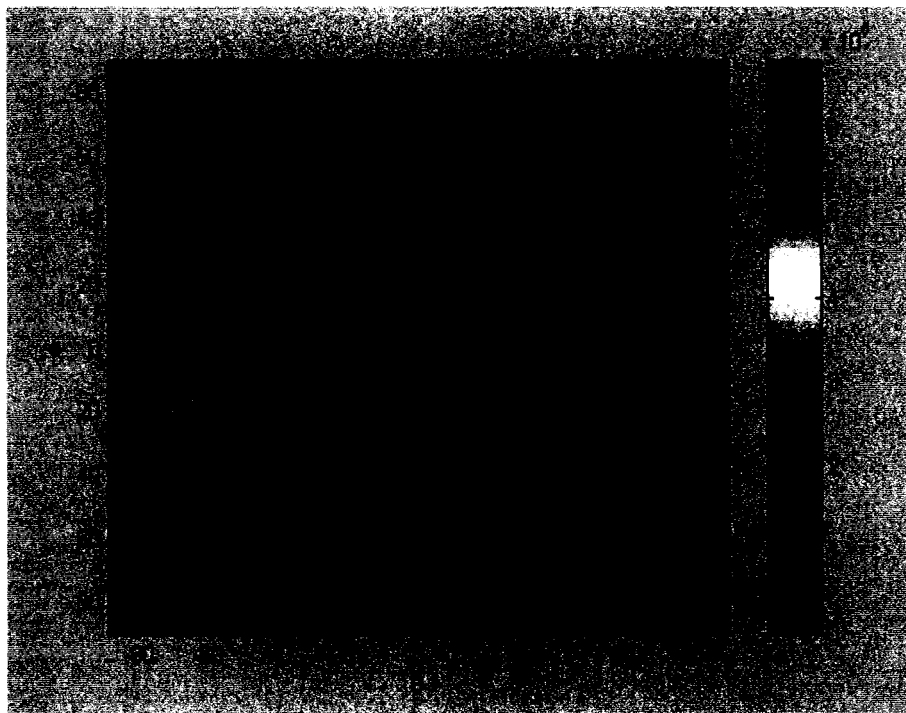


Figure 4.14: Map of dayside K^+ precipitation for the IMF case $[-43, 10, -10]$ at perihelion. Shown is the color-coded ion flux ($\text{cm}^{-2} \text{s}^{-1}$) in the case of an isotropic atmosphere. In this figure, as well as in the ones that follow, north is down, while dawn is at left.

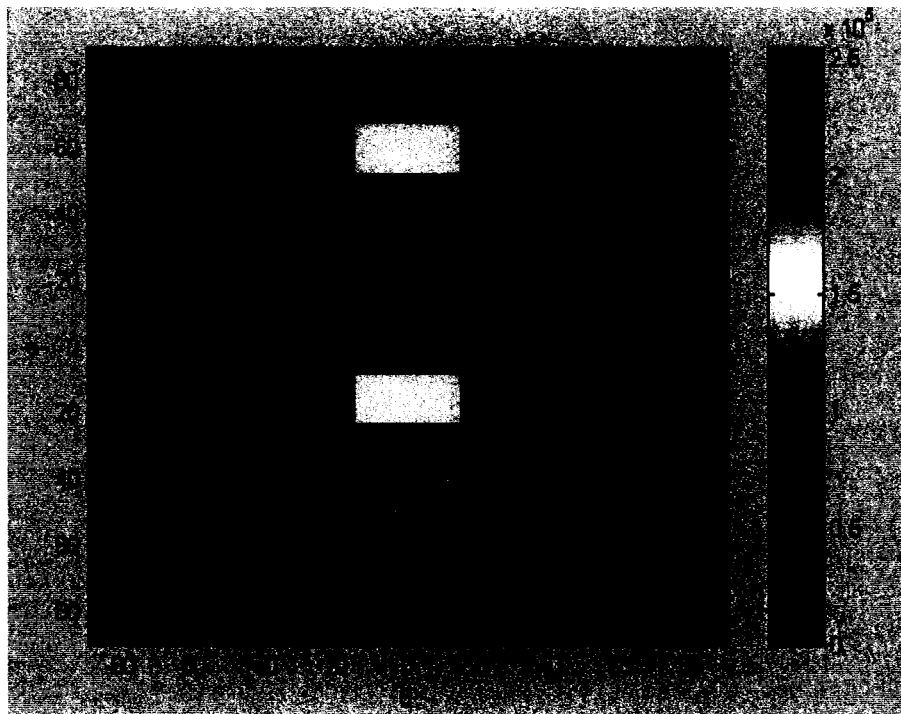


Figure 4.15: Map of K^+ dayside precipitation for an isotropic atmosphere at aphelion for IMF [-19, 5, -5].

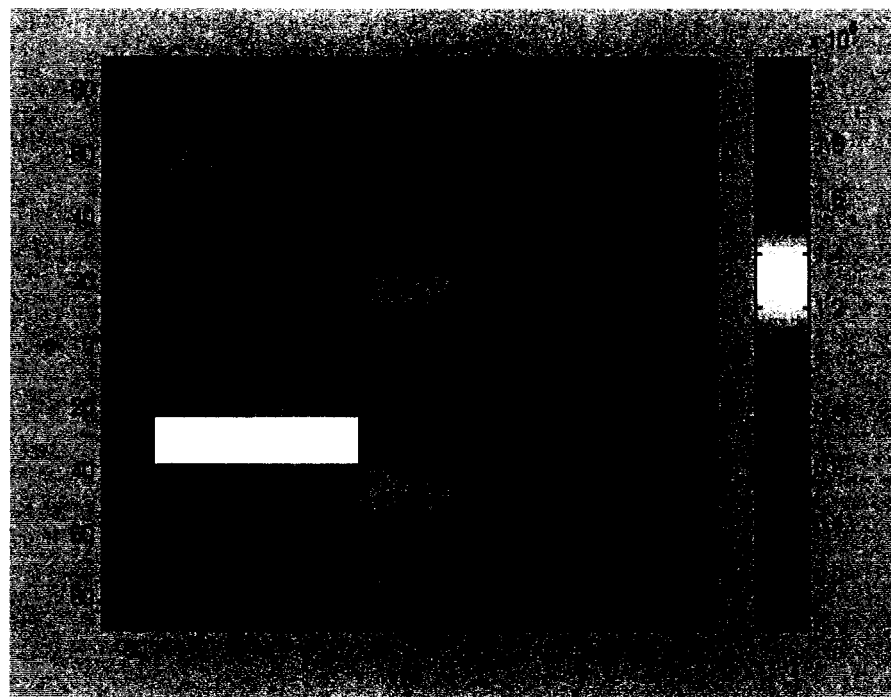


Figure 4.16: Map of dayside precipitation of potassium ions at aphelion for IMF [-10, 5, -10] in the case of an isotropic atmosphere.

4.5.2 The anisotropic atmosphere

Using the results of the isotropic distribution, we can make predictions about more plausible anisotropic atmospheric conditions. To this end, it is useful that we plot not where ions return, but where they are launched from and whether they neutralize or not. Specifically, what fraction of particles launched from each surface element impacts anywhere.

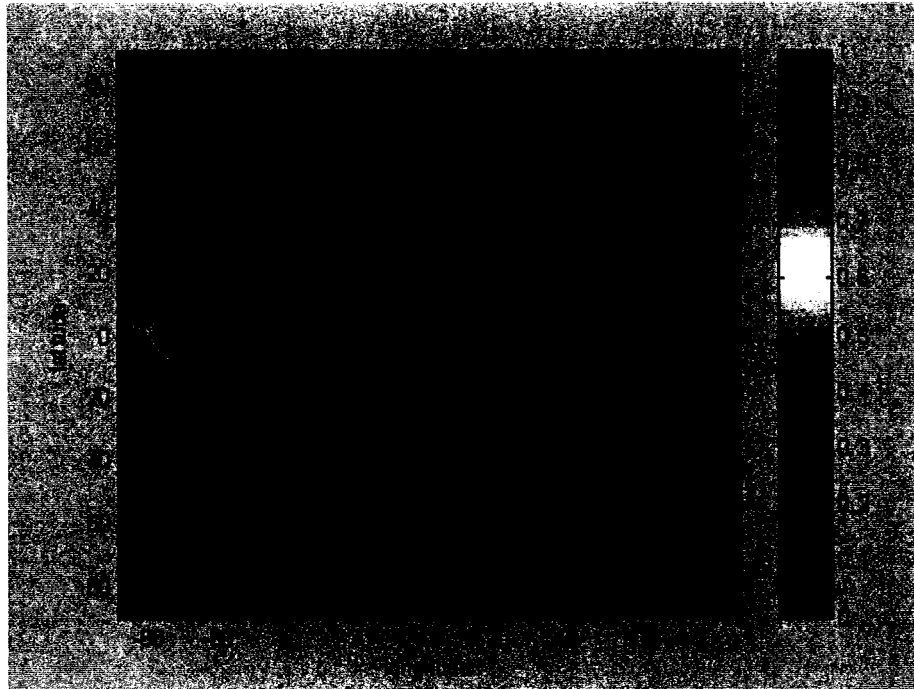


Figure 4.17: Fraction of sodium ions launched from each surface element that recycle anywhere on the surface for the isotropic atmosphere at perihelion with IMF $[-43, 10, -10]$ nT. Ions that are launched from the subsolar area predominantly escape to the solar wind. As a result, a realistic anisotropic atmosphere, which has a strong component around subsolar with added sharp peaks at mid latitudes, exhibits even lower recycling that the one computed in the isotropic case (see Table 3.6).

A realistic atmosphere varies roughly as $F_{SUB} \cos^{1/2} \phi \cos^{1/2} \vartheta$, where ϕ and θ are the launching latitude and longitude measured from the subsolar point. On this an ion sputtering component is superimposed at mid latitudes (40^0 - 60^0) as we will compute in the next chapter. Figure 4.17 shows that such an atmosphere has extremely low recycling rates ($\sim 35\%$) for sodium photoions at perihelion: the entire area around subsolar contributes ions that are getting swept away by the solar wind. In contrast, the aphelion cases exhibit very high recycling as seen in Figures 4.18, 4.19. Results are similar for potassium ions.

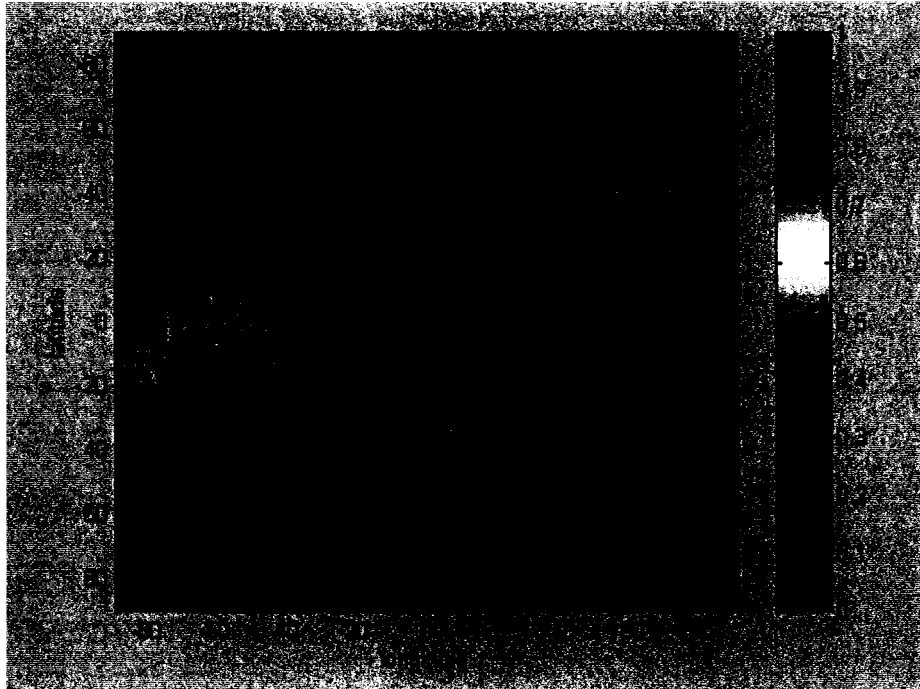


Figure 4.18: Fraction of sodium ions launched from each surface element that recycle anywhere on the surface for the isotropic atmosphere at aphelion with IMF [-19, 5, -5] nT. Because ions neutralize when they are launched from the dusk side (right side of plot) around the subsolar point, recycling in a realistic atmosphere at aphelion will be slightly higher compared to the isotropic atmosphere for these conditions.

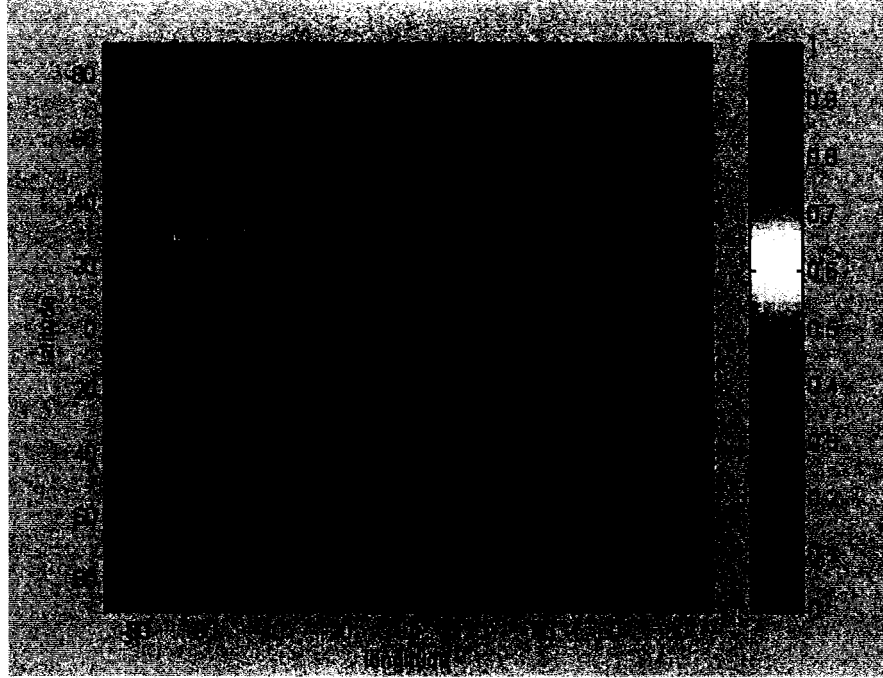


Figure 4.19: Fraction of sodium ions launched from each surface element that recycle anywhere on the surface for the isotropic atmosphere at aphelion with IMF [-10, 5, -10] nT. Conclusions for the anisotropic atmosphere for these conditions are the same as those in Figure 4.18.

	Perihelion	Aphelion, weak Bz	Aphelion, strong Bz
Global	48.4%	73.5%	86.7%
recycling (1)			
Effective	35.6%	66.8%	83.8%
recycling (2)			
Escape (3)	51.6%	26.5%	13.3%
Sputtering (4)	12.8%	6.7%	9.9%

Table 3.6: Fractional percentage of Na^+ particles that (1) returned to the surface; (2) returned with energies < 300 eV causing adsorption rather than sputtering or implantation; (3) escaped to the solar wind; and (4) caused sputtering for our three configurations in the case of an non-isotropic atmosphere. Here the atmosphere, as well as the initial ion distribution, was taken to vary as $F_{SUB} \cos^{1/2} \varphi \cos^{1/2} \vartheta$ with some solar wind ion sputtering happening at mid latitudes.

4.6 Implications of photoion tracings

While the global potassium simulations of this work are the first ever tried, a comparison exists between our sodium tracings and the paper by Delcourt et al. (2003). Comparing Figures 4.10, 4.11, and 4.20, we find that the perihelion cases appear similar, but that the aphelion cases differ significantly. The two perihelion cases feature a mid-latitude high flux band, although our case extends into a wider area of latitudes. These bands are symmetric in the Delcourt results, which do not include the Bx component, but asymmetric in the results of the TH93 model, which successfully incorporates Bx. The impact flux in our test is higher since we compute a 45% recycling rate against 15% which was earlier reported by Delcourt (Leblanc et al., 2003). On the other hand, in the aphelion case precipitation was spread over a wide area in our simulation. Contrary to what the Delcourt runs suggest, the morphology of ion redistribution in our results critically depends on the choice of the solar wind and IMF conditions.

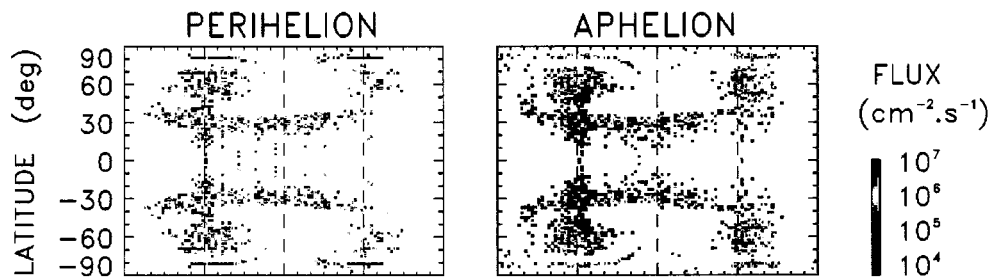


Figure 4.20: A comparison with the Delcourt (2003) sodium runs

The escape rate is found to respond to external conditions only loosely: between aphelion and perihelion, the escape ratio was seen to range from 30 to just 40 percent.

Therefore, impacts dominate. This result implies significant retention of volatiles in the regolith over geological times. While long-term recycling is very strong, it reduces by about a factor of 1.5 at perihelion. This prediction could help explain why the sodium atmosphere is denser at aphelion (Killen, personal communication).

The fraction of high-energy impacts, as well as the pattern of ion precipitation in the surface, is shown to respond to changes in the magnetosphere and the solar wind. Looking at Tables 3.4 and 3.5, the flux capable of sputtering is found to vary between 10-15 % of the entire dayside flux for strongly southward IMF $B_z = -10$ nT, but drops sharply in the $B_z = -5$ nT case.

What is the fraction of photoions that become trapped on the nightside and are accelerated toward the surface at high energies? We found that it varies depending on the solar wind and the IMF configuration. For potassium, almost all nightside impacts were energetic for the aphelion case with strong B_z , but almost none were so in the aphelion case with weak B_z . In general, when $B_z = -10$ nT, nightside sputtering rates varied between 7.5-10 % of the entire dayside flux, but when $B_z = -5$ nT, very little sputtering is seen. In the case of a quiet-time atmosphere, in which most ions are released from latitudes around the subsolar point, where the electric field is small, very little sputtering is seen in the nightside. Results were similar for sodium nightside impacts in the cases investigated here.

In fact, while we underline that the magnetosphere controls the recycling rate of photoions of each species on orbital scales, we note that there is no statistically significant difference between the fractional recycling rates for sodium and for potassium. To explain the variable Na/K ratio in the atmosphere, Potter et al. (2002)

suggested that recycling rates for potassium photoions will be lower than recycling rates for sodium photoions because potassium has a larger gyroradius in Mercury's magnetic field. However, we find no such evidence in the record of these global runs. Anticipating these conclusions, Killen et al. (2004) now believe that the variability of the Na/K ratio in the atmosphere may be controlled not by differential photoion losses, but by thermal diffusion in the grains: when a strong emission spurt drops the concentration in the grains below what is needed to support the atmosphere with 10^7 Na atoms $\text{cm}^{-2} \text{s}^{-1}$, sodium emissions rebound faster, but potassium emissions lag behind because its thermal diffusion coefficient is 100 times lower. The forecast that there do not exist differential losses for potassium ions such that can explain the variable Na/K ratio in the atmosphere (which ranges by a factor of three) is an important result of this work.

Table 3.7 summarizes our computations of ion sputtering due to photoions. To get a sputtering yield for magnetospheric ions, a weighted average yield of 0.1 per particle can be used. A comparison with photon-stimulated desorption yields, which average about 10^{24} particles per second, and with the solar wind ion sputtering flux, which will be computed in the next chapter of this work, determines that ion sputtering due to planetary Na and K is comparatively unimportant as a source mechanism. However, other species, such as Mg which is expected to dominate Mercury's exosphere and exoionosphere, may contribute significantly to the source atmosphere.

	$\text{Na}^+ \text{ (s}^{-1}\text{)}$	$\text{K}^+ \text{ (s}^{-1}\text{)}$
Perihelion	4.0×10^{22}	5.79×10^{20}
Aphelion, weak Bz	9.92×10^{21}	1.65×10^{20}
Aphelion, strong Bz	2.2×10^{22}	3.14×10^{20}

Table 3.7: Comparative sputtering yield averages for sodium and potassium ions.

CHAPTER 5:

TRACINGS OF SOLAR WIND IONS

5.1 Overview

In this section we backtrace solar wind particles in the northern hemisphere to determine the impact flux at locations on Mercury's surface. The integrated flux along the effective open area, which we calculate, gives a measure of how important ion sputtering is as a comparative source of Mercury's atmosphere, while the flux per unit surface will be compared to yields per surface element to determine whether ion sputtering can affect the local morphology of the atmosphere, and account for the observed high-latitude enhancements.

5.2 Predictions of solar wind precipitation fluxes

Using the Onsager method detailed in Chapter 3, solar wind protons are launched from locations of Mercury's northern hemisphere, from the surface upwards, every five degrees of latitude and ten degrees of longitude. Particles traced from each point of this grid have energies of 1, 3, and 5 keV, respectively, and pitch angles of 0, 10, 20, and 30 degrees with respect to the local magnetic field. Particles with larger pitch angles were assumed to return to the surface. This pitch angle limit is understood through the relation:

$$\sin^2 \alpha = B_{SUB} / B_{SURF} \quad (5.1)$$

where $B_{\text{SUB}}=100$ nT at the standoff distance and $B_{\text{SURF}}=350$ nT the surface field at Mercury. Having determined earlier that the lowest latitude at which crossings are detected is 40 degrees at perihelion, we launched 2,500 particles in the $40^{\circ} - 90^{\circ}$ northern latitude area. Particles that crossed the magnetopause farther than $2 R_M$ down the tail, which represent the flanks of the open field line area, were disregarded in the flux calculations. It is assumed that 50% of the magnetosheath plasma on reconnected field lines crosses the magnetosphere (Masetti et al., 2003). Following are maps of the realistic solar wind flux that impacts Mercury's surface in each of the three cases tested.

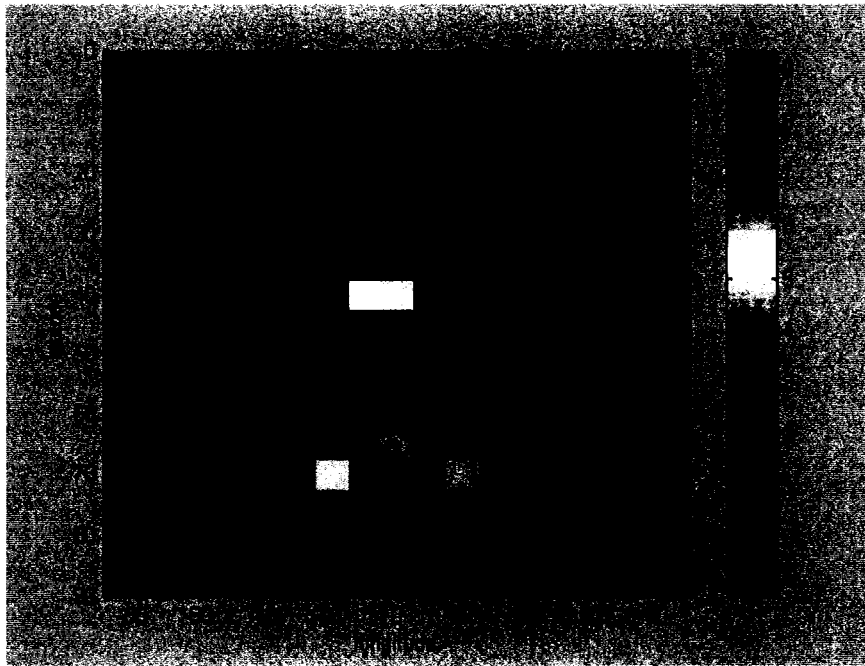


Figure 5.1: Color-coded flux ($\log(\text{cm}^{-2} \text{ s}^{-1})$) of solar wind ions that impact the surface of the Northern hemisphere at perihelion with IMF $[-43, 10, -10]$ nT. An extended impact area of high flux is found both behind the open-closed boundary (black line) and ahead of it, that is, along closed field lines.

As can be seen in Figs 5.1 through 5.3, these simulations confirm that at Mercury solar wind precipitation can happen not only along open, but also along closed field lines. These crossings along closed field lines happened not only at perihelion, as we expected, but also at aphelion. However, rather than reaching ~20 degrees into the closed field line area as Kallio and Janhunen (2003) predicted, our impacts extend the open-closed boundary to the closed field line area by about 5-7 degrees of latitude. Most of the flux capable of sputtering is deposited on a region that is limited in latitude but extended in longitude. The effective area that is open to the solar wind, that is, the area of non-zero flux, expands with increasing B_x .

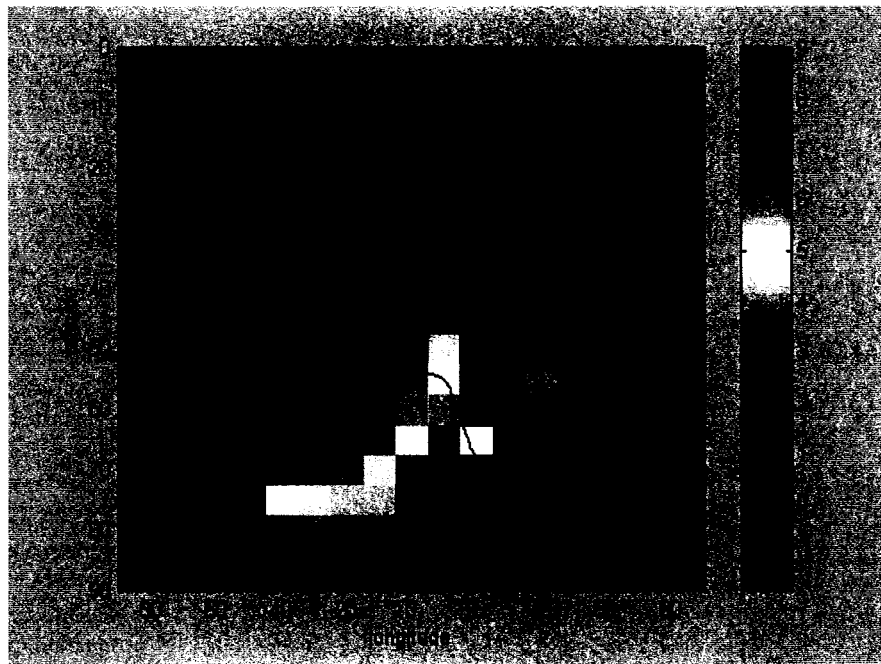


Figure 5.2: Color-coded flux ($\log(\text{cm}^{-2} \text{s}^{-1})$) of solar wind protons that impact the surface of the Northern hemisphere at aphelion with IMF $[-19, 5, -5]$ nT. Most of the flux impacts along the lower end of the cusp, while high-latitude fluxes are smaller.

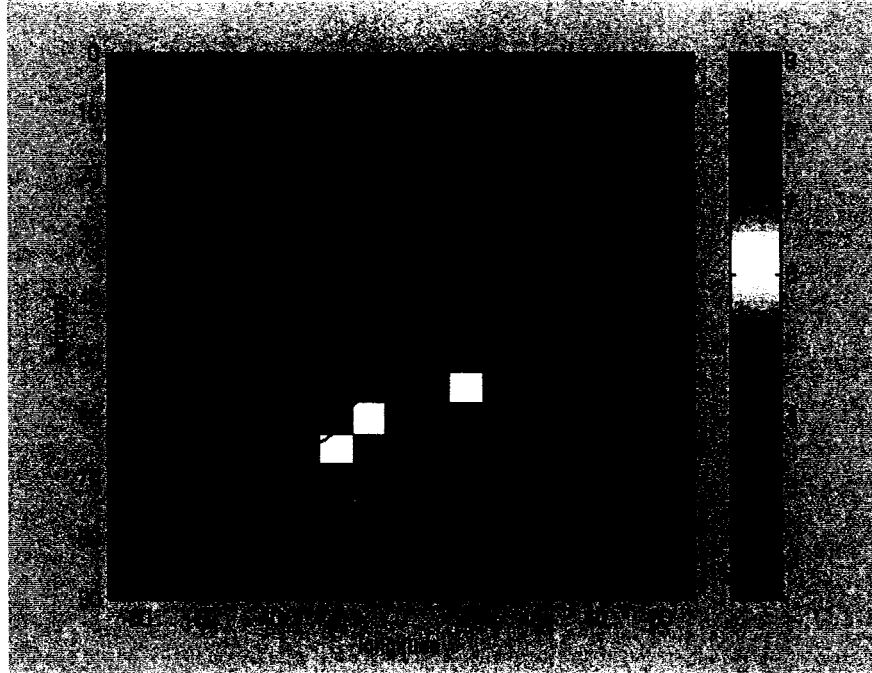


Figure 5.3: Color-coded flux ($\log(\text{cm}^{-2} \text{ s}^{-1})$) of solar wind H^+ that impact the surface of the Northern hemisphere at aphelion with IMF $[-10, 5, -10]$ nT. Impacts are now more symmetrically distributed because the IMF B_x and B_z are comparable.

5.3 Implications of the solar wind mapping for Mercury's atmosphere

Solar wind protons may not be responsible for solar wind sputtering, but may just be a proxy for sputtering caused by heavy ions in the solar wind (especially stripped ions), which have sputtering efficiencies orders of magnitude greater than that of protons. For example, while impacting solar wind protons produce 0.05 particles per impact, stripped oxygen ions (O^{+7}) sputter 500 particles per impact (Shemansky, 2003). To test whether contribution from heavies dominate the solar wind sputtering yield, we run O^{+7} ions having energy of 27 keV in Mercury's perihelion fields. Results are presented in Figure 5.4.

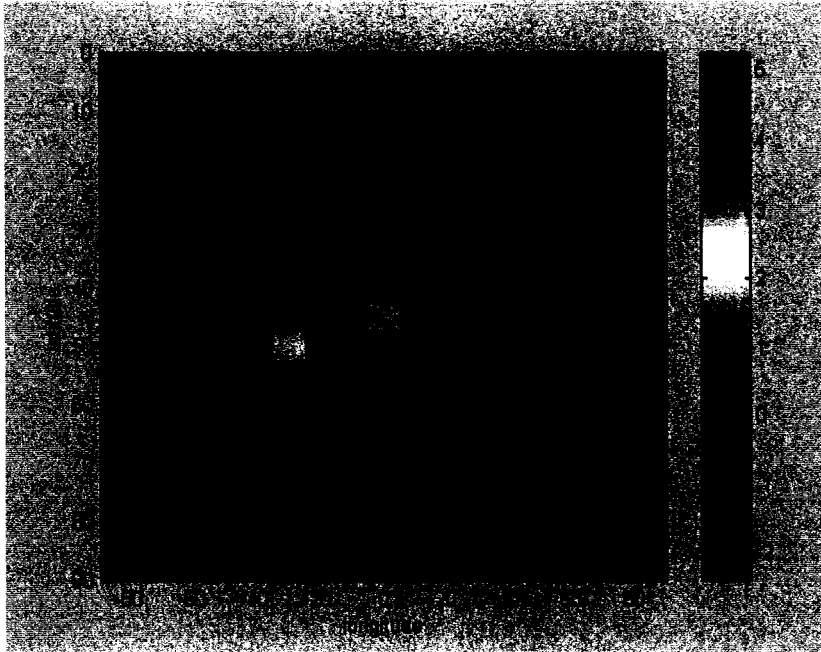


Figure 5.4: Color-coded flux ($\log(\text{cm}^{-2} \text{ s}^{-1})$) of solar wind O^{+7} ions that impact the surface of the Northern hemisphere at perihelion with IMF $[-43, 10, -10]$ nT. The sputtering flux of these ions is confined by the velocity filter effect to the lower edge of the cusp. Because of their increased sputtering efficiency, they contribute as many sputtered neutrals in that region as the more numerous solar wind protons.

In a planetary body without a magnetosphere, such as the Moon, these stripped oxygen ions yield 7 times more sputtered neutrals than solar wind protons: even though their relative abundance in the solar wind is 7×10^{-4} , their sputtering efficiency is 10^4 times higher than that of protons. But at Mercury, as Figure 5.4 attests, the magnetosphere, via the velocity filter effect, confines the heavy ion flux to the lower edge of the cusp. Thus, heavy ions in the solar wind do not dominate the sputtering yield at Mercury. Still, they may double the solar wind sputtering source as seen in Table 5.1. The effective temperature of these ions was assumed to be 3.2×10^7 K, or 16 times higher

than the temperature of solar wind protons. But if instead reconnection enlarges local temperature for heavies, the fluxes will be absorbed into a more extended area in latitude, resulting in even higher contributions from heavies. We plan to investigate this in the future.

Table 5.1 summarizes our computations of ion sputtering due to the solar wind. A weighted average yield of 0.05 per impacting particle is used to get a sputtering yield for protons, while the sputtering efficiency of stripped oxygen ions is assumed to be 500 (Shemansky, 2003). These sputtering yields are compared with yields of photon-stimulated desorption (PSD), which is believed to be the major source mechanism of the sodium and potassium atmosphere (e.g, Killen et al., 2001).

The effective open area, which is tabulated in column (2) of Table 5.1, increases to about 20% of the entire hemisphere in the perihelion run. The total sputtering flux integrated over this area, which extends into the closed field line region, is shown to increase by a factor of 1.5 between aphelion and perihelion for cases when the B_x is dominant. Since the PSD flux regularly increases by a factor of 2.3 from aphelion to perihelion, we predict that solar wind ion sputtering will be comparatively more important at aphelion than at perihelion. This result, coupled with the higher aphelion recycling predicted by our model, may help explain why the atmosphere is denser at aphelion (Killen, personal communication). With the inclusion of other heavy species that are present in the solar wind, ion sputtering can possibly account for 20% of all atmospheric content under southward IMF conditions.

	Effective open area (cm ⁻²)	Total sputtering flux (s ⁻¹)	Total sputtering yield (s ⁻¹)
perihelion			
H ⁺	2.52x10 ¹⁶	6.17x10 ²⁴	3.08x10 ²³
O ⁺⁷	1.55x10 ¹⁵	9.89x10 ¹⁹	4.94x10 ²²
aphelion, weak Bz			
H ⁺	1.43x10 ¹⁶	2.79x10 ²⁴	1.39x10 ²³
O ⁺⁷	1.40x10 ¹⁵	1.32x10 ²⁰	6.60x10 ²²
aphelion, strongBz			
H ⁺	2.18x10 ¹⁶	1.05x10 ²⁴	5.25x10 ²²
O ⁺⁷	1.40x10 ¹⁵	2.60x10 ¹⁹	1.32x10 ²²

Table 5.1: Effective open area, total sputtering flux, and total sputtering yield in the Northern hemisphere for the tests run in this study. The average yield per incident particle is assumed to be 0.05 for protons, and 500 for stripped oxygen ions. (Shemansky, 2003). For comparison, the yield for PSD is $5.5 \times 10^{24} \text{ cm}^{-2} \text{ s}^{-1}$ at perihelion, and $2.5 \times 10^{24} \text{ cm}^{-2} \text{ s}^{-1}$ at aphelion. With the inclusion of other heavy ions in the solar wind, ion sputtering may account for up to 20% of Mercury's sodium atmosphere.

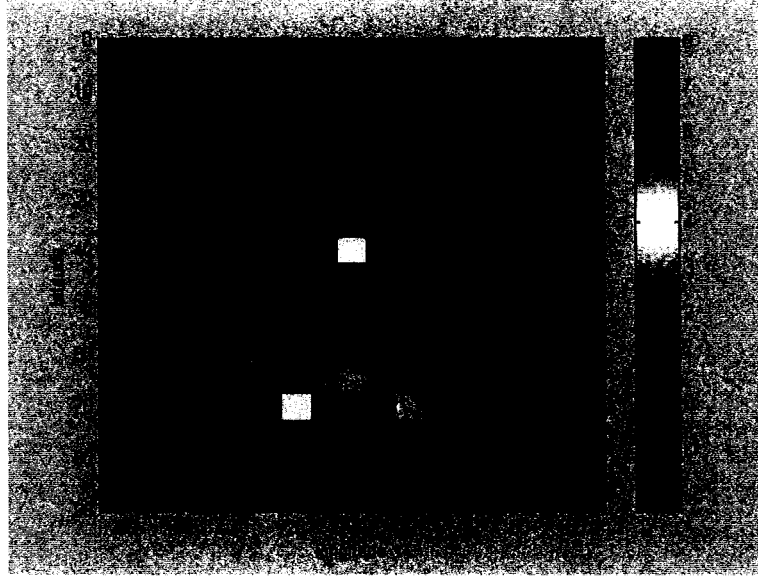


Figure 5.5: Color-coded sputtering yield ($\log(\text{cm}^{-2} \text{s}^{-1})$) due to precipitation of solar wind H^+ and O^{+7} ions in the Northern hemisphere at perihelion with IMF $[-43, 10, -10]$ nT. When these sputtering yields are inserted into a model of Mercury's atmosphere, they produce distinctive spikes of sodium column density in the area around the lower edge of the cusp (see Figure 5.6).

Solar wind sputtering dominates the high-latitude atmosphere when the IMF is southward. With computed particle yields in our model of 10^7 - 10^8 $[\text{cm}^{-2} \text{s}^{-1}]$ in latitudes around the open-closed boundary (Figure 5.5), ion sputtering due to the solar wind can increase surface yields by a factor of 100 over competing source mechanisms in this area. Indeed, the average surface yield to continuously support the content of 10^{28} sodium atoms in the atmosphere having a lifetime over photoionization of about 7 hours is:

$$\frac{10^{28} (\text{atoms})}{(2.52 \times 10^5 \text{ s}) (\pi R_M^2)} \approx 2 \times 10^5 \text{ Na cm}^{-2} \text{s}^{-1}$$

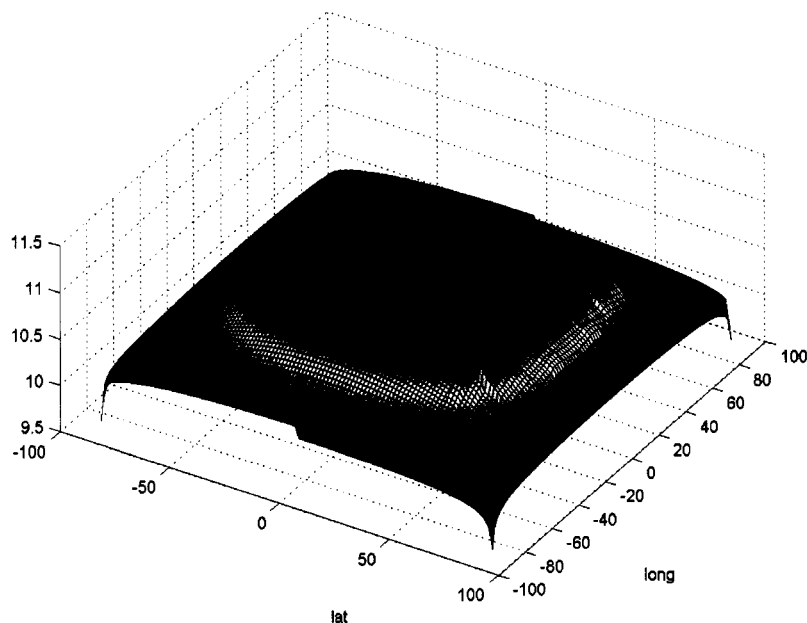


Figure 5.6: Color-coded sodium column density (cm^{-2}) at perihelion with IMF $[-43, 10, -10]$ nT. All source and loss processes are run concurrently. The ion sputtering source, in particular, is given by our model output (Figure 5.5). No ion sputtering was considered in the Southern hemisphere. The model has successfully reproduced the high-latitude enhancements seen in imaging data of the sodium atmosphere (Killen, personal communication)

The resulting atmosphere will therefore have enhancements at mid and high latitudes when the IMF is southward. Figure 5.6 presents the modeled sodium atmosphere when all source and loss processes are run concurrently (Killen, personal communication). This run, in which the solar wind ion sputtering yield is given by our model (Figure 5.5), confirms that sputtering by the solar wind can explain the high-latitude enhancements seen in imaging data.

CHAPTER 6:

SUMMARY

The modified version of the analytic Toffoletto-Hill (TH93) open magnetosphere model, supplemented by the Ding (1995) potential solver that computes the realistic electric potential that is self-consistent with the magnetic field, made possible tracings of solar wind and magnetospheric ions in Mercury's magnetosphere. Three cases of the solar wind and the interplanetary magnetic field (IMF) are tested: one perihelion with interplanetary magnetic field (IMF) $[-43, 10, -10]$, and two aphelion runs with IMF $[-19, 5, -5]$ and $[-10, 5, -10]$, respectively. Photoions are launched from the scale height for each species, while solar wind ions are ejected from the surface and traced upwards to the magnetopause.

6.1 Photoions

In these simulations, photoions can either escape to the solar wind or impact the surface. The computed escape rate to the solar wind responds to external conditions very little: between aphelion and perihelion, the escape ratio was seen to range from 30 to just 40 percent. Therefore, impacts dominate. This result implies significant retention of volatiles in the regolith over geological times. While long-term recycling is very strong, it

reduces by about a factor of 1.5 at perihelion. This prediction could help explain why the sodium atmosphere is denser at aphelion (Killen, personal communication).

Maps of ion precipitation produced in this work critically depend on the choice of solar wind and IMF conditions. Recycling sodium ions have fluxes high enough (10^6 – 10^7 $\text{cm}^{-2} \text{ s}^{-1}$) to enhance local surface yields by a factor of two when they impact at energies generally less than 300 eV. Coupled with this variable precipitation pattern in the dayside, photoions can affect the short-term morphology of the atmosphere. But when their impact energies are higher than that, they cause sputtering or implantation, and further raise surface yields. The flux capable of sputtering is found to vary between 10 to 15 % of the entire dayside flux for strongly southward IMF $B_z = -10$ nT. However, it typically represents only $10^{-1} - 10^{-3}$ of the computed solar wind ion sputtering flux, and must not feature in the long-term evolution of the atmosphere.

Concurrent tracings of sodium and potassium ions, which were investigated for the first time in this work, show that significantly higher escape losses do not exist for potassium photoions. Based on these results, we forecast that the variable Na/K ratio in the Hermean atmosphere, which ranges between 40 and 160 depending on the time of observation, is not explained by variable photoion losses. The most probable remaining mechanism to account for this variability is thermal diffusion from the regolith, which acts 100 times more efficiently on sodium than on potassium (Killen et al. 2004).

The modeled quiet-time atmosphere, that is, the atmosphere when no significant emission is seen due to either impact vaporization or ion sputtering, exhibits extremely high recycling and very few high-energy impacts. Because most of the photoions in these

cases are released from low latitude areas, where the electric field is small, little energization occurs.

6.2 Solar wind ions

In the second part of this study, we model the long-term variation of the solar wind ion sputtering flux. The total sputtering flux computed for realistic cases of southward IMF in this work is found to vary by about a factor of 1.6 between aphelion and perihelion for cases with dominant B_x . We predict that ion sputtering will be a comparatively strong source for Mercury's atmosphere under these conditions, accounting for about 20% of all atmospheric content then.

Our simulations confirm earlier predictions that, at Mercury, solar wind precipitation can happen not only along open, but also along closed field lines. These crossings along closed field lines happened not only at perihelion, as we expected, but also at aphelion, and must be a typical feature of southward IMF configurations at Mercury. Our impacts extend the open-closed boundary to the closed field line area by about 5-7 degrees of latitude. Heavy ions in the solar wind do not dominate the sputtering yields as previously thought (Shemansky, 2003). The sputtering flux of these ions is confined by the velocity filter effect to the lower edge of the cusp. Because of their increased sputtering efficiency, they contribute as many sputtered neutrals in that region as the more numerous solar wind protons.

Solar wind sputtering dominates the high-latitude atmosphere when the IMF is southward. Because the average computed particle flux in our model is about 1.7×10^8 $[\text{cm}^{-2} \text{ s}^{-1}]$, yields of 10^7 $[\text{cm}^{-2} \text{ s}^{-1}]$ are attained in latitudes around the open-closed boundary for southward IMF conditions. During these times sputtering due to the solar wind can increase surface yields by a factor of 100 over competing source mechanisms in this area. Therefore, the resulting atmosphere will have enhancements at mid and high latitudes when the IMF is southward. In future work we plan to couple the magnetosphere model with a model of Mercury's exosphere developed by Rosemary Killen, and model all source and loss mechanisms concurrently for specific datasets exhibiting such high latitude enhancements.

6.3 Future work

One such instance is the set of images collected from Nov. 13-20, 1997. In that week, the overall content of the sodium atmosphere increases by a factor of two, while high-latitude enhancements of brightness seem to shift from the southern to the northern hemisphere and then back. We now have at our disposal predictions of the solar wind and IMF configuration at Mercury during that week through a tomography model by Bernard Jackson, of University of San Diego, and through a solar MHD model developed by Tom Detman at NOAA (Figure 6.1). We plan to run our particle tracer with their input, compute the day-to-day variation of the solar wind flux that impacted Mercury's surface, then turn these results over to Killen to run through her atmosphere model. This will be

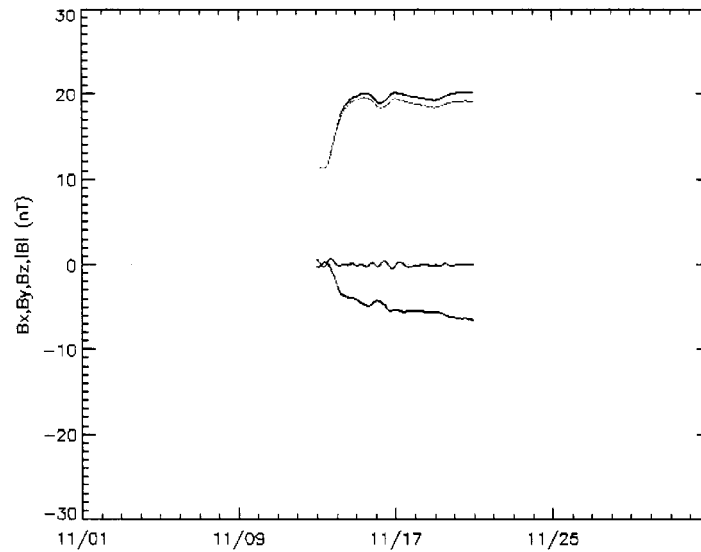


Figure 6.1: The IMF at Mercury during Nov. 13-20, 1997, predicted by the Detman solar MHD model (courtesy Tom Detman). Bx is red; By is black; Bz is blue. Because Mercury was close to the heliospheric current sheet during that time, model predictions for the IMF Bz are unreliable; yet they provide a good estimate of the other two IMF components.

the first ever specific event modeled through the coupled magnetosphere and atmosphere models.

While five types of magnetospheric models have been adapted to Mercury, no comparative studies have been forthcoming so far. With the collaboration of Michael Shay of University of Maryland, we intend to do a comparison of a hybrid model with the TH93 model for Mercury. This effort will relate the solar wind tracings of the TH93 model to results produced by Kallio and Janhunen (2003), which are controversial.

The NASA/MESSENGER mission to Mercury, which was launched last June, will get into orbit around Mercury in 2009. Because its orbit will be very eccentric, the

spacecraft will spend about a third of its time in the solar wind, making in situ measurements of the particles and fields in Mercury's environment. This will be the first time ever when images of Mercury's atmosphere will be matched with measurements of the prevailing solar wind and IMF, and will enable the magnetospheric community to test the validity of the adapted Mercury magnetosphere models by matching their predictions against the observed images of the atmosphere.

References

- Christon, S. P.; 1987, A comparison of the Mercury and Earth magnetospheres: electron measurements and substorm time scales, *Icarus*, 71, pp.448-471.
- Cowley, S. W. H., 1995, Theoretical Perspectives of the Magnetopause: A Tutorial Review, in *Physics of the magnetopause*, Geophysical Monograph 90, edited by P. Song, Bengt U. Ö., Sonnerup, and M.F.Thomsen. ISBN 0-87590-047-X, published by the American Geophysical Union, Washington, DC, 1995, p.29.
- Delcourt, D. C.; Moore, T. E.; Orsini, S.; Millilo, A.; Sauvaud, J.-A., 2002, Centrifugal acceleration of ions near Mercury, *Geophysical Research Letters*, Volume 29, Issue 12, pp. 32.1-32.3.
- Delcourt, D. C.; Grimald, S.; Leblanc, F.; Berthelier, J.-J.; Millilo, A.; Mura, A.; Orsini, S.; Moore, T. E., 2003, A quantitative model of planetary Na⁺ contribution to Mercury's magnetosphere, *Annales Geophysicae*, vol. 21, Issue 8, pp.1723-1736.
- Ding, C., 1995, Analytical and numerical modeling of the electromagnetic structure of geospace, PhD thesis, Rice University, Houston
- Dukes, C. A.; Baragiola, R. A., 2002, Contribution of Ion Sputtering to the Production of Na and K in the Lunar Atmosphere, in *The Moon Beyond 2002: Next Steps in Lunar Science and Exploration*, STI publication, p. 14.
- Hill, T. W.; Dessler, A. J.; Wolf, R. A., 1976, Mercury and Mars: The role of ionospheric conductivity in the acceleration of magnetospheric particles, *Geophysical Research Letters*, vol. 3, Aug. 1976, p. 429-432.
- Hill, T. W.; Reiff, P. H., 1977, Evidence of magnetospheric cusp proton acceleration by magnetic merging at the dayside magnetopause, *J. of Geophysical Research*, vol. 82, pp. 3623-3628.
- Huebner, W.F.; Keady, J. J.; Lyon, S. P., 1992, Solar Photo Rates for Planetary Atmospheres and Atmospheric Pollutants, *Astrophys. Space Sci.*, 195, pp. 1-294.
- Ip, W. -H., 1987, Dynamics of electrons and heavy ions in Mercury's magnetosphere, *Icarus*, vol. 71, p. 441-447.

Ip, W.-H., 1993, On the Surface Sputtering Effects of Magnetospheric Charged Particles at Mercury, *Astrophysical Journal*, v.418, p.451.

Ip, W.; Kopp, A., 2002, MHD simulations of the solar wind interaction with Mercury, *J. of Geophysical Research (Space Physics)*, Volume 107, Issue A11, pp. SSH 4-1.

Kabin, K.; Gombosi, T. I.; DeZeeuw, D. L.; Powell, K. G., 2000, Interaction of Mercury with the Solar Wind, *Icarus*, Volume 143, pp. 397-406.

Kallio, E.; Janhunen, P., 2003, Solar wind and magnetospheric ion impact on Mercury's surface, *Geophysical Research Letters*, Volume 30, Issue 17, pp. SSC 2.1-2.4.

Killen, R. M.; Morgan, T. H., 1993, Maintaining the Na atmosphere of Mercury, *Icarus*, Volume 101, Issue 2, p. 293-312.

Killen, R. M.; Ip, W.-H., 1999, The surface-bounded atmospheres of Mercury and the Moon, *Reviews of Geophysics*, Volume 37, Issue 3, p. 361-406.

Killen, R. M.; Potter, A. E.; Reiff, P.; Sarantos, M.; Jackson, B. V.; Hick, P.; Giles, B., 2001, Evidence for space weather at Mercury, *J. of Geophysical Research*, Volume 106, Issue E9, p. 20509-20526.

Killen, R. M.; Potter, A.E.; Sarantos, M.; Reiff, P., 2003, Recycling of Ions in Mercury's Magnetosphere, 25th meeting of the IAU, Joint Discussion 2, 16 July, 2003, Sydney, Australia, meeting abstract.

Killen, R. M.; Sarantos, M.; Potter, A. E.; Reiff, P., 2004, Source rates and ion recycling rates for Na and K in Mercury's atmosphere, *Icarus*, Volume 171, Issue 1, p. 1-19.

Leblanc, F.; Johnson, R. E., 2003, Mercury's sodium exosphere, *Icarus*, Volume 164, Issue 2, p. 261-281.

Leblanc, F.; Delcourt, D.; Johnson, R. E., 2003, Mercury's sodium exosphere: magnetospheric ion recycling, *J. of Geophysical Research*, Volume 108, Issue E12, pp. 10-1.

Luhmann, J. G.; Russell, C. T.; Tsyganenko, N. A., 1998, Disturbances in Mercury's magnetosphere: Are the Mariner 10 "substorms" simply driven?, *J. of Geophysical Research*, Volume 103, Issue A5, p. 9113-9120.

Masetti, S.; Orsini, S.; Milillo, A.; Mura, A.; de Angelis, E.; Lammer, H.; Wurz, P., 2003, Mapping of the cusp plasma precipitation on the surface of Mercury, *Icarus*, Volume 166, Issue 2, p. 229-237.

Ness, N. F.; Behannon, K. W.; Lepping, R. P.; Whang, Y. C., 1975, The magnetic field of Mercury, part 1, *J. of Geophysical Research*, 80, pp. 2708-2716.

Ogilvie, K. W.; Scudder, J. D.; Vasyliunas, V. M.; Hartle, R. E.; Siscoe, G. L., 1977, Observations at the planet Mercury by the plasma electron experiment - Mariner 10, *J. of Geophysical Research*, vol. 82, May 1, 1977, p. 1807-1824.

Onsager, T. G.; Kletzing, C. A.; Austin, J. B.; Mackiernan, H., 1993, Model of magnetosheath plasma in the magnetosphere - Cusp and mantle particles at low-altitudes, *Geophysical Research Letters*, vol. 20, no. 6, p. 479-482.

Onsager, T. G.; Chang, S.W.; Perez, J. D.; Austin, J. B.; Janoo, L. X., 1995, Low-altitude observations and modeling of quasi-steady magnetopause reconnection, *J. of Geophysical Research*, vol. 100, no. A7, p. 18,831-18,843.

Potter, A. E.; Morgan, T. H., 1990, Evidence for magnetospheric effects on the sodium atmosphere of Mercury, *Science*, vol. 248, p. 835-838.

Potter, A. E.; Morgan, T. H., 1997, Sodium and potassium atmospheres of Mercury, *Planetary and Space Science*, v. 45, p. 95-100.

Potter, A. E.; Killen, R. M.; Morgan, T. H.; 1999, Rapid changes in the sodium exosphere of Mercury, *Planetary and Space Science*, Volume 47, Issue 12, p. 1441-1448.

Potter, A. E.; Anderson, C. M.; Killen, R. M.; Morgan, T. H., 2002, Ratio of sodium to potassium in the Mercury exosphere. *J. of Geophysical Research (Planets)*, Volume 107, Issue E6, pp. 7-1.

Reiff, P.H.; Luhmann, J.G., 1986, Solar wind control of the polar-cap voltage, in *Solar wind-magnetosphere coupling*, Proceedings of the Chapman Conference, Pasadena, CA, Feb. 12-15, 1985 (A87-40101 17-46). Tokyo/Dordrecht, Terra Scientific Publishing Co./D. Reidel Publishing Co., 1986, p. 453-476.

Russell, C. T.; Baker, D. N.; Slavin, J. A., 1988, The magnetosphere of Mercury, in *Mercury*, ISBN 0-8165-1085-7, University of Arizona Press, Tucson, AZ, 1988, p. 514-561.

Sarantos, M.; Reiff, P.H.; Hill, T. W.; Killen, R. M.; Urquhart, A. L., 2001, A B_x -interconnected magnetosphere model for Mercury, *Planetary and Space Science*, Volume 49, Issue 14-15, p. 1629-1635.

Shemansky, D. E., 2003, The role of solar wind heavy ions in the space environment, in *Rarified Gas Dynamics: 23rd International Symposium*, AIP Conference Proceedings, Volume 663, p. 687-695 (2003).

Slavin, J. A.; Holzer, R. E., 1979, The effect of erosion on the solar wind stand-off distance at Mercury, *J. of Geophysical Research*, vol. 84, May 1, 1979, p. 2076-2082.

Smyth, William H.; Marconi, M. L., 1995, Theoretical overview and modeling of the sodium and potassium atmospheres of the moon, *Astrophysical Journal*, Part 1 (ISSN 0004-637X), vol. 443, no. 1, p. 371-392.

Sprague, A. L.; Kozlowski, R. W. H.; Hunten, D. M.; Schneider, N. M.; Domingue, D. L.; Wells, W. K.; Schmitt, W.; Fink, U., 1997, Distribution and Abundance of Sodium in Mercury's Atmosphere, 1985-1988, *Icarus*, Volume 129, Issue 2, pp. 506-527.

Sprague, A. L.; Schmitt, W. J.; Hill, R. E., 1998, Mercury's sodium atmospheric enhancements, radar-bright spots, and visible surface features, *Icarus*, Volume 136, Issue 1, pp. 60-68.

Toffoletto, F. R.; Hill, T. W., 1989, Mapping of the solar wind electric field on the earth's polar caps, *J. of Geophysical Research*, vol. 94, p. 329-347.

Toffoletto, F. R.; Hill, T. W., 1993, A nonsingular model of the open magnetosphere, *J. of Geophysical Research*, vol. 98, no. A2, p. 1339-1344.

Vasyliunas, V. M., 1983, Large-scale morphology of the magnetosphere, in *Solar-terrestrial physics: Principles and theoretical foundations; Proceedings of the Theory Institute, Chestnut Hill, MA, August 9-26, 1982 (A84-33851 15-46)*, Dordrecht, D. Reidel Publishing Co., 1983, p. 243-254.

Voigt, G.H., 1981, A mathematical magnetospheric field model with independent physical parameters, *Planetary and Space Science*, Volume 29, Issue 1, p. 1-20.

Xue, S., 1996, Numerical modeling of the magnetospheric cusp: ion injection and number density calculations, PhD thesis, Rice University, Houston.

Whang, Y. C., 1977, Magnetospheric magnetic field of Mercury, *J. of Geophysical Research*, vol. 82, p. 1024-1030.